

This Supplemental Material accompanies Ross, C.M., and Kavscek, A.R., 2022, Nanometer-scale pore structure and the Monterey Formation: A new tool to investigate silica diagenesis, *in* Aiello, I., Barron, J., and Ravelo, C., eds., Understanding the Monterey Formation and Similar Biosiliceous Units across Space and Time: Geological Society of America Special Paper 556, [https://doi.org/10.1130/2022.2556\(04\)](https://doi.org/10.1130/2022.2556(04)).

Nanometer-Scale Pore Structure and the Monterey Formation: A New Tool to Investigate Silica Diagenesis: *Supplemental Materials*

Cynthia M. Ross¹ and Anthony R. Kavscek¹

¹*Energy Resources Engineering, Stanford University, 367 Panama St., Stanford, CA 94305-4007*

CONTENTS

Procedures and Development

- Sample Preparation
- Outgassing
- Isotherm Acquisition
- Data Processing
- Quality Control

Summary of Experimental Effects

- Interpretation of the First Peak
- Experimental Effects on the Second Peak

Silica Groups

- Example SEM Textures and Spectra
- Interpreted Silica Groups

Comparison with Other Work

Additional SEM Image and Pore Structure Examples

Additional SEM Images

Acknowledgments

References

PROCEDURES AND DEVELOPMENT

Detailed procedures and development information for the nitrogen sorption methodology used to characterize silica diagenesis follows. This method focuses on the nanometer-scale porosity (< 300 nm throat size) associated with opal-CT. The methodology consists of five steps: (1) sample preparation, (2) outgassing, (3) isotherm acquisition, (4) data processing, and (5) quality control. This information is more comprehensive than presented in Ross et al. (2016).

Sample Preparation

Representative samples are cut using a rotary saw and cleaned to remove soluble hydrocarbons. Cleaning consists of repeated soaks in toluene at room temperature. Samples are soaked for at least three days. If the toluene is discolored, it is replaced, and the process is repeated until the toluene remains clear. Once clean, the toluene is drained off, and the sample is allowed to air dry in the fume hood. After drying, the samples are then shaped using 1500 grit sandpaper into mini cores that are about ~ 8 mm in diameter by 5 to 15 mm in length (Fig. S1). This allows the mini cores to fit into the 9-mm interior-diameter sample cells. Drilling mini cores was not an option, because the majority of samples are either too friable or too brittle. Sorption measurements for this study require ~10–30 hrs with samples having substantial nanometer-scale pore volumes (i.e., opal-CT samples) requiring the most analysis time. If needed, mini cores containing mostly opal-CT were shortened (e.g., 5 mm) to reduce instrument time and guarantee sufficient liquid nitrogen was available to complete each run. For all mini core lengths, the entire sample fits within the cold zone for ideal measurement conditions. It is important to note that mini cores are not universally suitable for sorption analyses as indicated by comparisons of sieved samples with mini cores for Barnett and Eagle Ford shale samples (Ross, unpublished).



Figure S1. Example mini cores. Samples shown are quarry (opal-A), D 1341.1 (opal-A), A 1017.0 (opal-CT), and C X524.3 (diagenetic quartz). Letters indicate the sample source (quarry or field). Their assigned silica group is provided in parentheses. Scale is in cm. More information about the sample sources and silica groups are in Ross and Kovsky (2022).

Alternate sample preparation methods were tested, namely sieved disaggregated samples (63–125 μm , 125–150 μm , 150–250 μm , and 250 μm –2 mm) in addition to the mini cores. All of the test samples generate the same Barrett-Joyner-Halenda (BJH; Barrett et al., 1951) peak locations with differences only in the pore volumes associated with the peaks. Peak heights of the mini core, 250 μm –2 mm, and 125–150 μm samples correspond to each other (~ 0.0085

cm³/g/nm) whereas 63–125 µm and 150–250 µm are smaller (0.0067 and 0.0059 cm³/g/nm, respectively). These differences may be due various factors including mineral segregation by size and porosity loss via disaggregation. For the disaggregated samples, determining their mass is problematic in that the sample cells are too long to be fully enclosed within the balance. The use of mini cores avoids this issue as they can be readily removed from the cell for weighing. Mini cores have additional benefits in that they can be reanalyzed without sample loss, and cell cleanup is easy.

Outgassing

A low-temperature outgassing procedure with a maximum temperature of 50 °C is performed under vacuum prior to sorption measurements to remove adsorbed gases and water from the sample. Outgassing is critical to obtain accurate and repeatable results. The low temperature is required to minimize irreversible alteration of the sample. A typical outgassing process prior to sorption measurements consists of a series of user-defined temperature ramps (°C/min) up to a user-defined temperature and left to “soak” at that temperature for a user-defined period of time. The temperature is progressively increased to avoid “steaming” or structural damage due to the vaporization of water held in micropores (Lowell et al., 2004). The ideal outgassing routine is hot enough to desorb water and gases from the surfaces yet cool enough that minerals (such as clays and opal-A) and organic matter are not altered. Organic matter is especially sensitive to heating and may be chemically altered at temperatures as low as 30 °C (Tourtelot, 1979). Although hydrocarbons are typically generated at temperatures 70 °C and above, their formation may begin at temperatures as low as 50 °C (Tourtelot, 1979). In addition, clays and amorphous silica are susceptible to low temperature alterations from the dewatering of clay interlayers (e.g., Mielenz et al., 1953) and opals (e.g., Zhuravlev, 2000; Smallwood et al., 2008), respectively. The ideal maximum outgassing temperature must avoid chemically altering the sample and yet provide a consistent starting point for the sorption measurements (Sing et al., 1985).

Relatively pure diatomite (quarry) samples were outgassed at 50 and 250 °C for comparison. The samples were visibly altered after the 250 °C outgassing in that the original and 50 °C outgassed samples are buff colored whereas samples outgassed at 250 °C are gray. The peaks for the pore throat size distributions occur at the same pore throat size (~ 3.8 nm) for samples outgassed at both temperatures; however, the resulting nPSD peaks have greater volumes for samples outgassed at 250 °C. It could be argued that greater outgassing temperatures merely removed water from 3.7–3.9 nm-sized pores. This is not the case as the change is irreversible in that rehydration and time does not revert the high temperature sample back to its original state in subsequent runs. This is also true for diatomaceous samples outgassed at a more moderate 110 °C. In unpublished work by Ross, outgassing temperatures of 110 and 250 °C on immature mudstones resulted in thick coatings of organic matter in the glass cell. These observations indicate that both biosilica and organic matter are susceptible to alteration at temperatures of 110 °C and greater.

The recommended method of determining the optimal outgassing temperature is to run thermogravimetric analysis (TGA) and identify temperature intervals where the sample weight is consistent or has the least slope (Sing et al., 1985). Prior to TGA analysis, samples are typically dried at about 100 °C; therefore, changes are not observed in the TGA data until temperatures greater than 100 °C are achieved. Typical outgassing temperatures encountered in the literature (≥ 100 °C) also contribute to subsequent mismatches between pore throat size distributions derived from nitrogen sorption versus mercury injection (e.g., Kuila and Prasad, 2013; Ross, unpublished). To avoid this in our TGA measurements, a reduced-temperature preparation method was developed for diatomaceous rock types, their alteration products, and other mudstone types. These samples were not oven dried prior to outgassing and are subjected to a stepped 10-hour low temperature outgassing regimen with a maximum temperature of 50 °C. TGA measurements on quarry and clay-rich opal-A samples outgassed at 50 °C reveal consistent weights at temperatures up to 95 °C, thereby providing a stable starting weight for sorption measurements (Fig. S2). Exposure to 50 °C for 10 hrs could potentially alter organic matter and silica; however, this temperature is at or less than the natural reservoir temperatures for many of the study samples. Smallwood et al. (2008) tested outgassing gem opals at 50 °C for 24 hrs and found that opal-A samples lost 60% of their water mass whereas opal-CT samples were comparatively unaffected with a 2% loss. In light of this, reduced outgassing temperatures such as either 30 or 40 °C may be an option for future study. This is discussed further in the quality control section. The temperature outgassing methodology with a maximum temperature of 50 °C for 10 hrs was used prior to sorption analysis for all of the study samples.

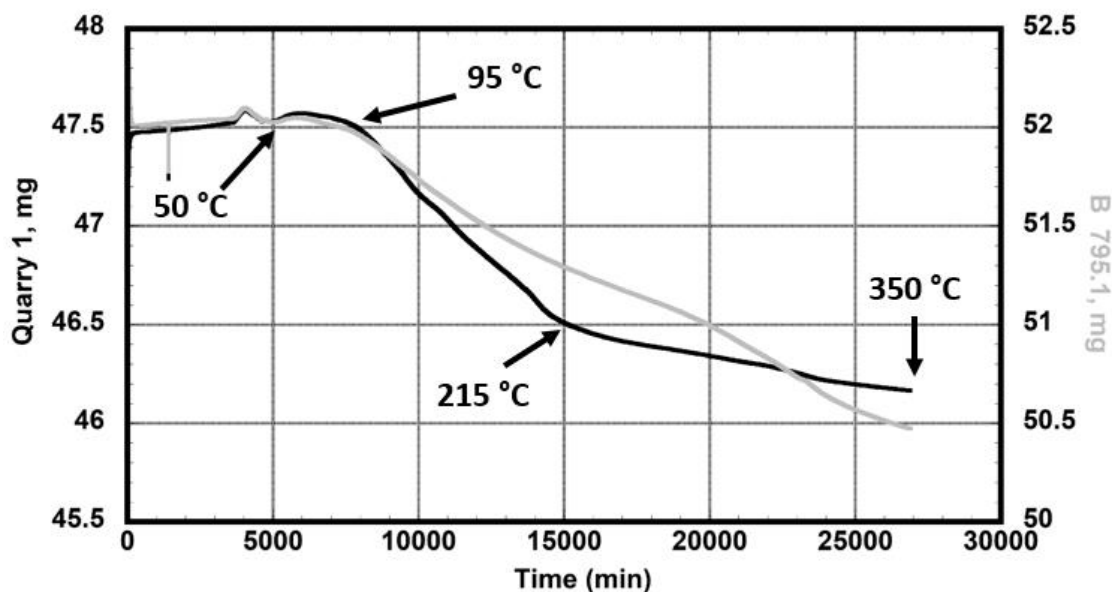


Figure S2. Thermogravimetric analysis measurements on quarry and Field B opal-A group samples. Mass loss versus time from 50 to 350 °C after simulated outgassing for 10 hrs at 50 °C in a nitrogen atmosphere.

Isotherm Acquisition

Sorption isotherms indicate the amount of gas, in this case nitrogen, adsorbed to sample material as the relative pressure increases (Fig. S3, light gray) followed by the amount of desorption as the relative pressure decreases (Fig. S3, dark gray) while cooled in a liquid nitrogen bath (-195°C). Relative pressure is calculated using the pressure measured for the cell containing the sample divided by the pressure measured on a reference cell that does not contain sample material; both cells are subjected to the same experimental conditions. The resulting isotherms are plotted as unitless relative pressure versus nitrogen volume (cm^3/g) at standard temperature and pressure (STP). Adsorption may be either physical (physisorption) consisting of weak intermolecular forces (such as van der Waals interactions) or chemical (chemisorption) with the formation of stronger bonds (Klobes et al., 2006). For this study, the amount of nitrogen gas adsorbed depends upon physical adsorption on pore surfaces (surface area) and capillary condensation (pore filling; Barrett et al., 1951). Hysteresis occurs when the desorptive branch deviates from the adsorptive branch (Fig. S3). For this application, hysteresis shape differs between samples depending upon either the presence or absence of opal-CT (Fig. S3). During adsorption or as relative pressure increases, pores of all sizes are filled from the pore walls inward. During desorption or as relative pressure decreases, drainage is controlled by pore throat sizes. This effect has been likened to a movie theater experience. Before the movie, people leisurely enter and select a seat. After the movie when everyone is leaving at the same time, your departure is then controlled by the size of the exits. In this way, desorptive isotherms are used to measure nanometer-scale surface area (nSA), pore volume (nPV), and pore throat size distribution (nPSD). An “n” differentiates these nanometer-scale pore characterization parameters from those measured on total porosity including the porosity accessed via pore throat sizes greater than ~ 300 nm.

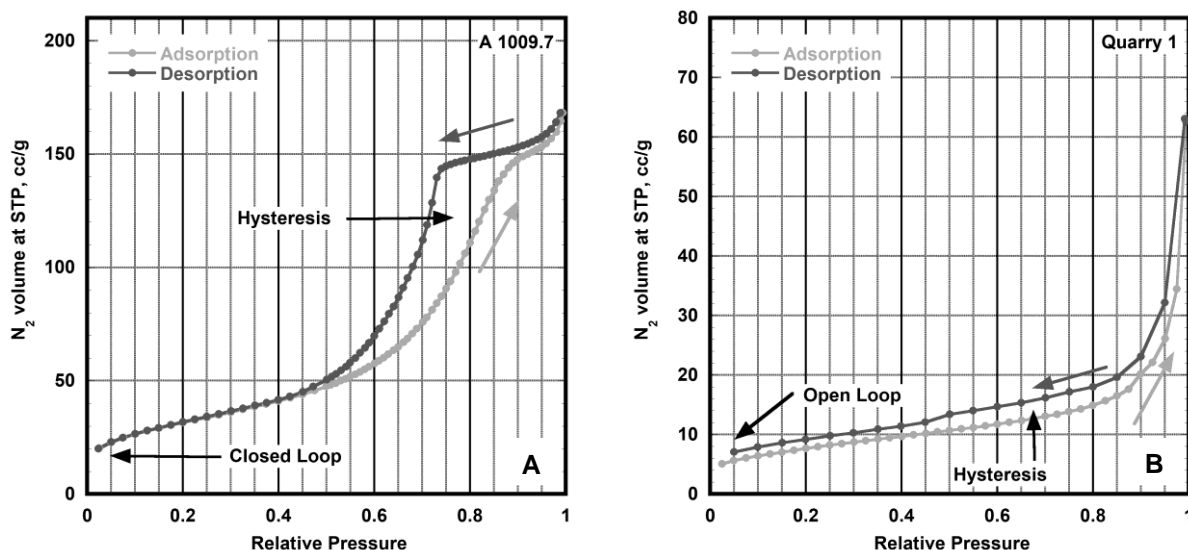


Figure S3. Example nitrogen isotherms for (A) an opal-CT sample (~ 60 wt% XRD) collected with 70 points for each isotherm and (B) an opal-A sample with 40-point adsorptive branch and

20-point desorptive branch. (A) The lower number of data points collected for the opal-A sample results in an open loop. Notice the different scales for the vertical axes. STP – Standard temperature and pressure.

Isotherms should have closed loops in which the two branches coincide with each other at lower relative pressures (Fig. S3). Adsorption and desorptive measurements with 20, 40, 55, and 70 points were tested. For this study, 70 points are collected on both adsorptive and desorptive branches of the isotherms. The large number of points serves two purposes: (1) the increased number of increments facilitates better filling and drainage of the pores (i.e., closed hysteresis loops) and (2) allows for better matches when plotting the nPSD results with mercury injection porosimetry (MIP) data. This is discussed further in the following section. All nitrogen sorption measurements are performed using Quantachrome Autosorb iQ3 systems, and excess space is excluded using filler rods in 9-mm bulbless cells.

Data Processing

Many models exist for calculating size distributions from nitrogen isotherms. These models assume different substrates and pore shapes as well as use different branches (adsorption vs desorption) and segments (relative pressure ranges) of the isotherms. When the output of these methods is compiled, multitudes of unique pore throat size distributions (nPSD) represent the same isotherm or sample. Some examples including BJH and density functional theory (DFT) for different isotherms and substrates (silica and carbon) are shown in Figure S4A. For this application, the optimal model, the BJH method (Barrett et al., 1951), provides the best fit (with respect to peak location, peak height, and peak volume) to the same pore throat size interval from MIP-derived PSDs measured on corresponding samples (Fig S4C; additional examples Fig. 1 in Ross and Kovscek, 2022). In the example in Fig. S4C, the porosities for 0–60 nm pore throat size are 0.134 cm³/g for MIP and 0.132 cm³/g for BJH. To obtain this proper match, the isotherms are collected with 70 points for each branch (Fig. S4B). The nPSD data are resampled such that data point locations (pore throat sizes) of the nPSD and PSD distributions align. This requires summing the incremental pore volumes for the smallest pore throat sizes (< 20 nm) in the BJH distribution and, to a lesser extent, for 50–300 nm for the MIP data (Figs. S4B–S4C).

The BJH method calculates the desorption rate of nitrogen from cylindrical pores based on the Kelvin equation using the relative pressure portion of the isotherm greater than 0.35 (Barrett et al., 1951). It is important to note that the cylinder diameter is equivalent to the pore throat diameter and not the larger pore body diameter. The de Boer method (de Boer et al., 1966) is used to calculate the thickness of the nitrogen adsorbed to the pore walls. The BJH method was developed with the assumption of cylindrical pores using bone char and tested on activated carbon, silica gel, and clay cracking catalyst (Barrett et al., 1951). A subsequent paper by Joyner et al. (1951) compared the nPV and nPSD of BJH analysis to MIP measurements with good agreement. They limited the applicability of their method to pore throat diameters of 60 nm or smaller.

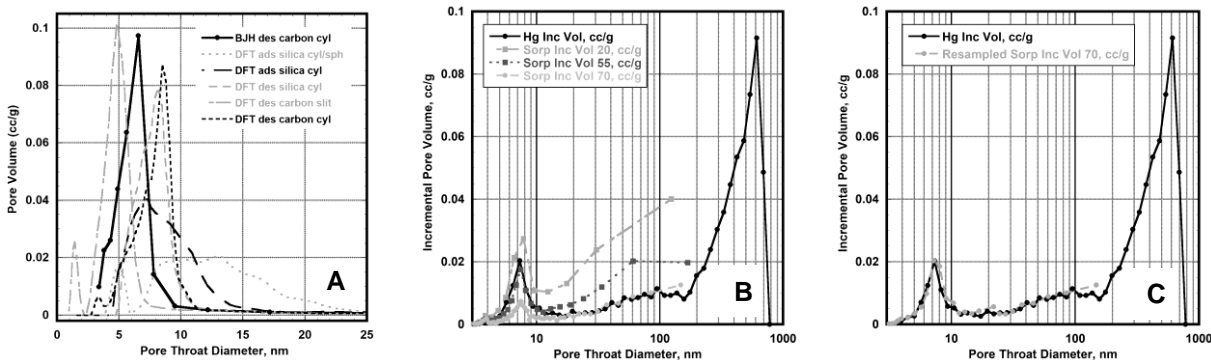


Figure S4. Pore throat diameter versus incremental pore volume for opal-A to opal-CT transition sample, B 1420.5. (A) A subset of sorption models and parameters (showing only 0–25 nm throat size range), (B) comparison of mercury injection and nitrogen sorption (BJH processing) with 20, 55, and 70 measurement points per isotherm branch, and (C) resampled 70-point sorption data and mercury injection data. The legend for the sorption model comparison plot (A) includes model (BJH or DFT), isotherm branch (adsorption or desorption), substrate (carbon or silica), and pore shape(s) (cylinder, sphere, and/or slit).

In this study, BJH nPSDs and MIP PSDs correspond with each other from about 3.9 or 8 nm depending on the maximum pressure of the MIP measurement (60,000 or 33,000 psi, respectively) and up to 90–200 nm in diameter depending upon the quality of the fit (Fig. 1 in Ross and Kavscek, 2022). The only exceptions occur in Field C samples with comparatively high pore volumes ($\geq 0.025 \text{ cm}^3/\text{g}$) for pore throat sizes between 30 and 100 nm in diameter. Nitrogen did not completely fill the volume of these pore throat sizes during the sorption measurements affecting both nPV and nPSD. For these samples, BJH pore throat size distribution is truncated as MIP data more accurately represent this portion of the PSD. In light of this, the nPV for Field C samples are less than their actual volume. The effects of this are presented in the Synthesis and Discussion section in Ross and Kavscek (2022).

Pore throat size distributions can be plotted as pore throat diameter versus incremental pore volume and differential pore volume with respect to pore throat diameter or $dv(d)$ (Fig. S5A). For comparison between sorption and MIP data, incremental pore volume was used as the relative pore volume filled through nanometer- and macro-scale pore throat sizes are not distorted (e.g., Fig. S5B). To identify subtle differences in the nanometer-scale pore structure for the purposes of silica phase interpretation, $dv(d)$ is preferred in that it emphasizes the nanometer-scale pores and diminishes the contribution as well as the complexity introduced by macro-scale pores (Fig. S5A). In this example, the viewer's eye is drawn to the peak heights and locations for pores between 5 and 10 nm in diameter for the $dv(d)$ plot (Fig. S5A) whereas the incremental plot commands more attention in the 100 nm pore throat size range (Fig. S5B). In addition, the zero porosity values at ~200 nm in the incremental plot are due to maximum pore throat size limitation of the BJH calculations for this sample (Fig. S5B). When combined with pore throat size distributions derived from mercury injection, these larger peaks merge with macroporosity peaks as viewed in Figures S4C and 1 in Ross and Kavscek (2022).

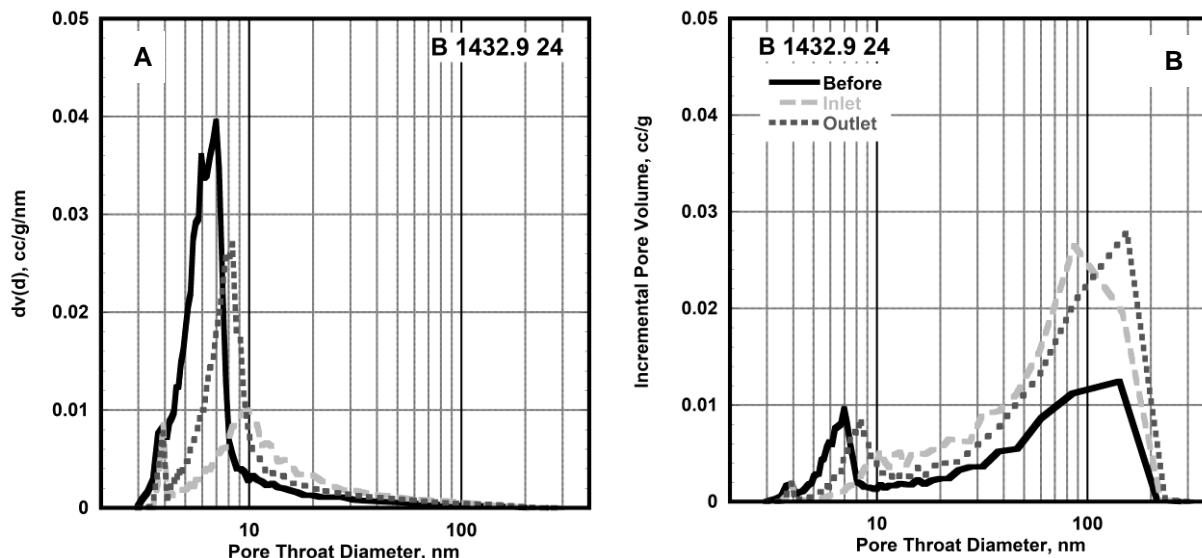


Figure S5. Comparison of pore throat diameter plotted against (A) differential pore volume with respect to pore throat diameter or $dv(d)$ in $\text{cm}^3/\text{g}/\text{nm}$ and (B) incremental pore volume in cm^3/g for the same data set. The key applies to both images. Original sample measurements are solid black lines. Measurements made after heated experiments conducted under flow conditions are from the inlet (dashed light gray lines) and outlet (dotted gray lines) ends of the core (Ross et al., 2016). The greatest amount of change occurred at the inlet.

Quality Control

Duplicate measurements were run on the same mini core to assess the consistency of the sorption measurements and multiple mini cores from the same sample to determine the heterogeneity of individual samples. For an opal-CT sample with alternating layers, different mini cores from the same sample (E 1363.7) yield a wide range of nSA ($130\text{--}214 \text{ m}^2/\text{g}$) and nPV ($0.106\text{--}0.392 \text{ cm}^3/\text{g}$). This sample is discussed further in the text (Ross and Kovscek, 2022). In contrast, three different mini cores were prepared for A 762 (opal-A) with resulting ranges of $19.0\text{--}22.3 \text{ m}^2/\text{g}$ and $0.172\text{--}0.189 \text{ cm}^3/\text{g}$, two mini cores from A 1015 (opal-CT) have ranges of $172.2\text{--}173.2 \text{ m}^2/\text{g}$ and $0.255\text{--}0.256 \text{ cm}^3/\text{g}$, and two samples selected to characterize visually distinct regions of C X541.2 (opal-CT to quartz transition) have ranges of $137.8\text{--}145.9 \text{ m}^2/\text{g}$ and $0.215\text{--}0.227 \text{ cm}^3/\text{g}$. In this case, mini core selection does not impact the interpretation of the sorption results provided visible heterogeneities within samples have been tested.

Comparison of repeated analyses run on the same mini core or replicates demonstrate the reproducibility of the measurements. For the replicates, the standard deviation is between 0.044 and $3.187 \text{ m}^2/\text{g}$ with an average of $1.069 \text{ m}^2/\text{g}$ for nSA and between 0.0007 to $0.041 \text{ cm}^3/\text{g}$ with an average of $0.014 \text{ cm}^3/\text{g}$ for nPV. The greatest percentage range occurs in samples with minimal pore volumes and surface areas. This is particularly true for opal-A and some opal-A to opal-CT transition group samples in which nPV and nSA tend to increase somewhat with each outgassing procedure. For example, the first run on B 1432.9 generated values of $83.0 \text{ m}^2/\text{g}$ and

0.187 cm³/g whereas the second run yielded values of 84.0 m²/g and 0.201 cm³/g. This is consistent with the observations of Smallwood et al. (2008). To minimize this drift effect, the first run for each mini core is preferred. For mini cores exposed to multiple outgassing procedures, the resulting sorption data remained in range for its silica group despite the slight drift.

SUMMARY OF EXPERIMENTAL EFFECTS

Over a period of 20 years, a variety of experiments were conducted on diatomaceous samples. Nitrogen sorption measurements were conducted on the samples before and after the experiments in order to detect changes in the nanometer-scale pore structure as an indication of silica alteration. Based on these experiments, we can see the effect of various conditions (temperature, flow, duration, etc.) on the nanometer-scale pore structure. A summary of the observations for the first and second peaks for the nPSD follow. More detailed information is available in Ross et al. (2016).

Interpretation of the First Peak

The first nPSD peak (3.7–3.9 nm) in silica samples can indicate either dissolution or extreme temperature exposure (either extra high temperatures or long duration) depending on experimental conditions as presented in Ross et al. (2016). Comparison of the first peak before and after experiments reveal increased peak height corresponding to high temperature exposure whereas decreased peak height and missing peaks occur after dissolution. Further work is needed to understand the mechanisms of change associated with this first peak as samples such as B 794.3 exhibiting dissolution via the first peak also have indications of silica alteration (i.e., initial signs of opal-CT formation) from increased pore volumes in the developing second peak (Fig. S6A).

For B 794.3, the sample was filled with a neutral brine, saturated with crude oil, and then flooded with synthetic boiler effluent (pH 10; Test 3 in Ikeda et al., 2007). Over the course of this experiment, the sample was held at 45°C and greater with a maximum temperature of 200 °C for almost five days. The experiment increased the total matrix porosity and generated channels from the inlet to the outlet of the core (Ross et al., 2008). In addition, dissolution was prevalent as indicated by ICP analysis of effluents produced during the experiments. For the nanometer-scale porosity, the first peak is almost eliminated compared to the measurement performed before the experiment (Fig. S6A). This change was also observed in a quarry sample filled with deionized water at room temperature (not shown, Q P4 in Ross et al, 2016; Peng and Kavscek, 2011). The loss of or reduction of its first peak is also attributed to dissolution. A field sample, E 823.9, was missing the first peak and was later found to be in close proximity to thermal enhanced recovery operations (Fig. A1J in Ross and Kavscek, 2022).

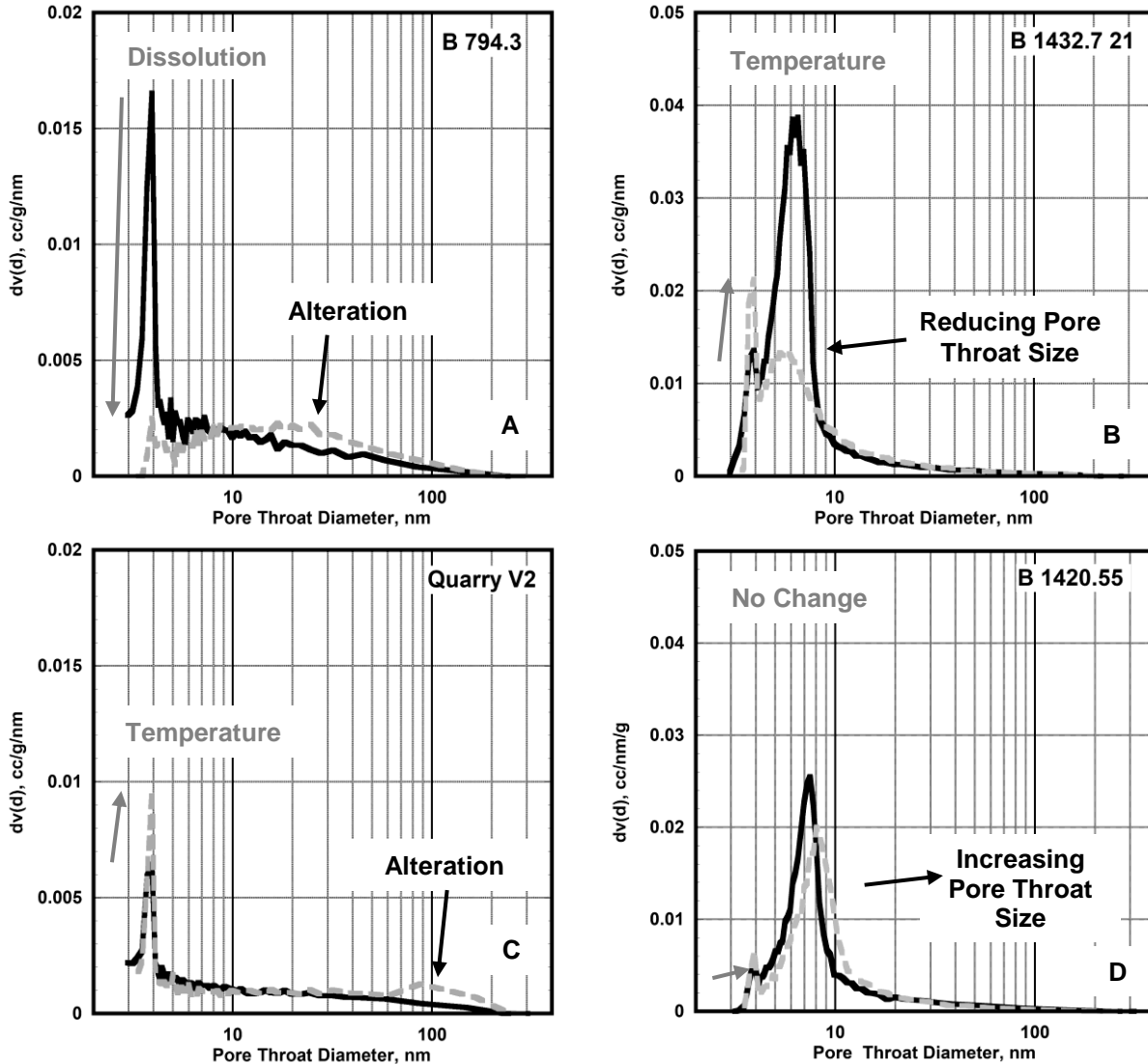


Figure S6. Examples of nPDS before (solid black line) and after experiments (inlet – light gray dashed line). Sample and core/experiment labels are included. Arrows and comparison comments before and after the experiments for the first peaks are in gray whereas the second peaks are in black. Vertical scales differ between plots with maximum $dv(d)$ values of $0.02 \text{ cm}^3/\text{g}/\text{nm}$ for opal-A group samples (A,C) and $0.05 \text{ cm}^3/\text{g}/\text{nm}$ for opal-A to opal-CT transition group samples (B,D).

Increases in the 3.7 to 3.9 nm or first peak were observed for some experiments as shown for B 1432.7 in Figure S6B. This core was filled with a brine and crude oil while conducting relative permeability measurements at 45, 120, and 230 °C for 818 days (Vega and Kovscek, 2014). As a result, the height of the first peak increases indicating that temperature effects were greater than dissolution with respect to the first peak. This effect was also observed in samples heated without flow (Q V2 in Fig. S6C; Q V3 and Q PS6 in Ross et al., 2016).

Experimental Effects on the Second Peak

Comparison of nPSD measured before and after experiments improves our understanding of the second peaks as well. A quarry sample, Q V2, was filled with neutral deionized water and then synthetic boiler effluent (pH 10) at 45 up to 230 °C for 7.5 days without flow (Ross et al., 2016; Vega et al., 2011). Before the experiment, the sample has only one peak. A second peak at about 60 to 200 nm is present after the experiment (Fig. S6C). This development was observed in all experiments on quarry samples conducted without fluid flow. Without fluid flow, silica concentrations would increase within the core judging from silica concentrations produced under flow conditions (e.g., Ikeda et al., 2007; Peng and Kavscek, 2011). In addition, nPV and nSA increase after experiments conducted under static conditions. In comparison, nPV and nSA decreased when quarry samples were subjected to fluid flow (Ross et al., 2016). Under experimental conditions, flow continually introduces fluids containing no silica in solution, thereby, contributing to dissolution and inhibiting precipitation.

The nPV-nSA behavior of the field samples is more complicated. This may be due, in part, to the greater range of experimental conditions and increased compositional heterogeneity between the samples (Ross et al., 2016). In the nPSD plots, the height of the second peak was reduced and, in some cases, the nanometer-scale pore throat sizes increased (Figs. S6B and S6D). Dissolution, a slight reduction in pore throat size, and a substantial reduction in peak height is indicated for B 1432.7 21 after the 818 day experiment (Fig. S6B). In contrast, B 1432.9 24 exhibits shift toward larger pore throat sizes with the greatest change occurring at the inlet compared to the outlet (Fig. S5A; Ross et al., 2016). This sample was filled with brine, saturated with crude oil, and heated to 45 °C and up to 230 °C for 83 days (Vega and Kavscek, 2010). This is also true for B 1450.55 that was exposed to 45 °C to a maximum of 230 °C for 2.8 days (Fig. S6D; Ikeda et al., 2007). For B 794.3, a second peak developed at 20 to 30 nm whereas the first peak diminished after the experiment (Fig. S6B; Ross et al., 2016).

SILICA GROUPS

Example SEM Textures and Spectra

Scanning electron microscopy (SEM) textures are determined using low magnification backscattered electron (BSE) images of polished surfaces of impregnated samples. Samples that are predominantly composed of opal-A (opal-A and opal-A to opal-CT transition group examples; Figs. S7A–C) are readily distinguished from samples consisting of mostly opal-CT (opal-CT and opal-CT to quartz transition group examples; Figs. S7D–S7E) using the textures revealed in low magnification images (Table 2 in Ross and Kavscek, 2022). Clay-rich opal-A samples cannot be distinguished from opal-A to opal-CT transition samples using the low resolution SEM images (Figs. S7B–S7C, Field B examples). The texture observed in opal-A and opal-A to opal-CT transition samples (Figs. S7A–S7C) is referred to as opal-A SEM texture (Table 2 in Ross and Kavscek, 2022). In the opal-CT, diagenetic quartz, and their transition

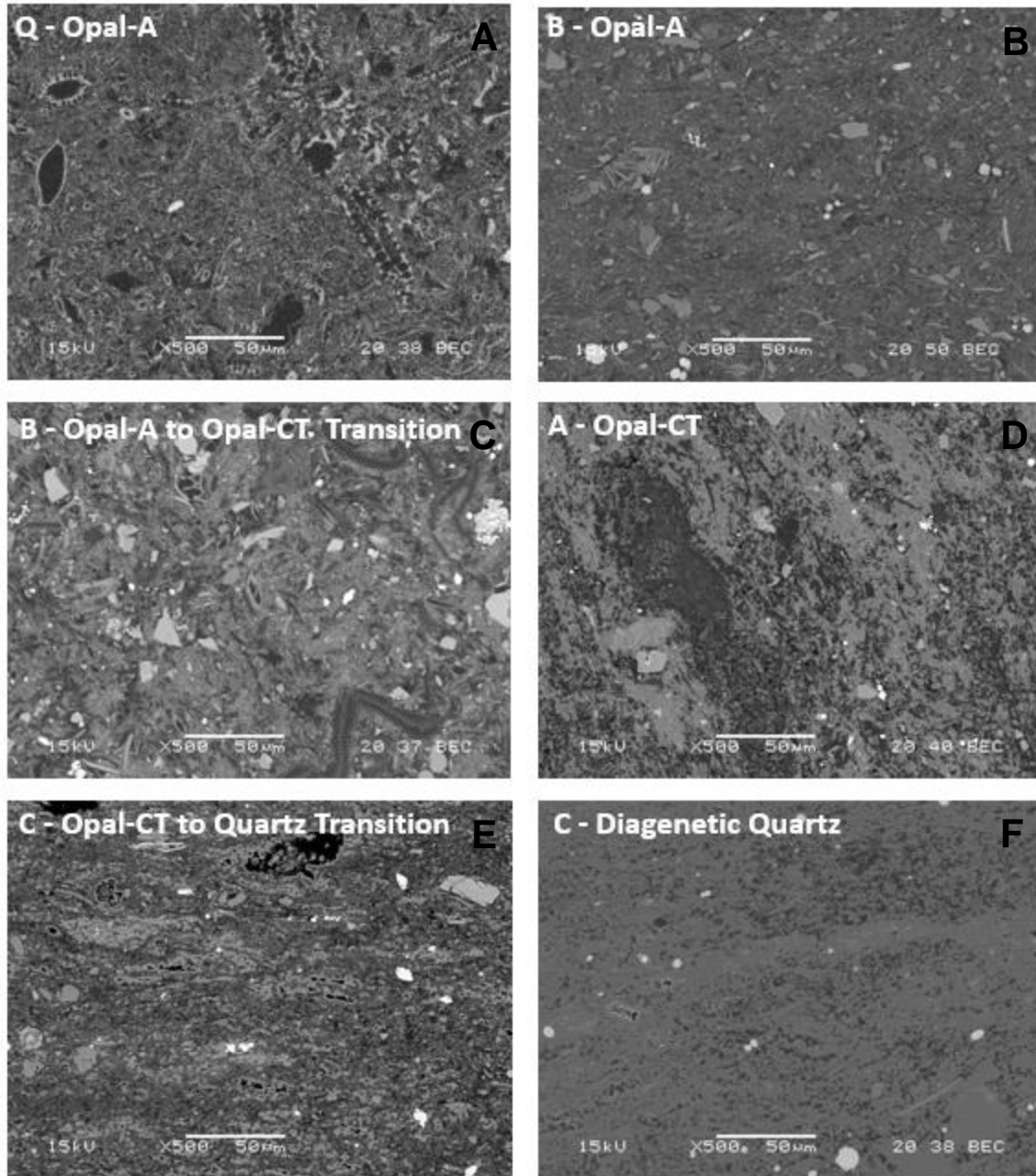


Figure S7. Scanning electron microscopy (SEM) backscattered electron photomicrographs of epoxy-impregnated polished samples representing each silica group as listed on individual images. SEM texture classifications for these example images are (A–C) opal-A SEM texture for opal-A and opal-A to opal-CT transition groups, (D–E) opal-CT SEM texture for opal-CT and opal-CT to quartz transition groups, and (F) diagenetic quartz SEM texture for diagenetic quartz group. Sample sources (letters) are listed on the upper left of each image. Field B examples are clay-rich. Epoxy-filled pores are black. Dark gray matrix regions represent mixed mineral and porosity response. Scale bars are 50 μm .

group samples (Figs. S7D–S7F, Fields A and C examples), intermediate grayscale values of the matrix reflect the relative amount of unresolved porosity with more porous regions being darker gray than less porous regions. This occurs when the pore size is less than the effective pixel size (resolution) yielding pixels that represent both mineral and epoxy-filled porosity. Clays can contribute to this effect, but these samples contain very little clay (< 3 wt%; Table 3 in Ross and Kovscek, 2022). The diagenetic quartz silica group example is referred to as having a quartz SEM texture (Fig. 7F); it is distinct from the opal-CT and opal-CT to quartz transition group examples that exhibit an opal-CT SEM texture (Figs. 7D–7E). The SEM textures for each silica group are labeled accordingly in Table 2 (in Ross and Kovscek, 2022) with example images available in Figure S7. These textures help assign silica groups for samples lacking quantitative XRD data as presented in the following section.

Interpreted Silica Groups

Thirty samples lack quantitative XRD data used to classify the other 29 samples by silica group (Table S1; Tables 2, 3, and 5 in Ross and Kovscek, 2022). In lieu of this data, these samples were classified based on XRD spectra (Fig. S8), FTIR spectra (e.g., Fig. S9), quantitative XRD measurements on adjacent samples (a few feet apart within the same stratigraphic interval in the same well), mercury injection or MIP-derived pore throat size distribution (Fig. 1 in Ross and Kovscek, 2022), SEM texture (Fig. S7), and SEM imaging of grain mounts. This section details how each sample in Table 5 (Ross and Kovscek, 2022) was assigned to its silica group. These interpreted silica group memberships are supported by the sorption data results in that they are similar to their equivalent known silica group samples. The samples are presented in order of silica maturity beginning with opal-A samples and ending with the opal-CT to quartz transition sample (Table 5 in Ross and Kovscek, 2022). The detrital quartz sample that was added for comparison to the diagenetic quartz group was not assigned to a silica group.

All quarry samples exhibit opal-A SEM texture and lack opal-CT peaks in XRD spectra. Field A samples, A 752.1, A 754.3, A 756.6, A 758.4, A 760.2, and A 764.0, were grouped with opal-A samples due to their opal-A texture in SEM images. Although opal-A to opal-CT transition group samples also have an opal-A texture in low-magnification SEM images of polished epoxy-embedded surfaces (Fig. S7), quantitative XRD on A 762.0 from the same interval confirms the opal-A group membership (Table 3 in Ross and Kovscek, 2022). As viewed in grain mounts, A 1563.6 contains abundant diatom frustules and was assigned to the opal-A silica group. The XRD spectrum verifies that the sample does not contain detectable amounts of opal-CT (Fig. S10A). Also, A 1596.8 from about 9 m (30 ft) deeper in the same well did not contain detectable opal-CT via spectral and quantitative XRD (Fig. S10B; Table 3 in Ross and Kovscek, 2022). The XRD spectrum of B 1498.7 I does not show signs of opal-CT (Fig. S10C). SEM images reveal opal-A frustules as well as unique morphologies (botryoidal silica) associated with high-temperature silica deposition (Fig. A2 in Ross and Kovscek, 2022). This sample was assigned membership in the opal-A silica group. All of the samples from Field D

exhibit an opal-A SEM texture in polished, impregnated mounts. Two samples with quantitative XRD, D 1341.1 and D 1484.9, do not contain detectable opal-CT (Table 3 in Ross and Kovscek, 2022). For samples with MIP data, none of the opal-A group samples exhibit nanometer-scale porosity associated with opal-CT.

TABLE S1. SAMPLE COUNT PER SILICA GROUP AND SOURCE

Silica Group*	Quarry	A	B	C	D	E
<u>XRD/FTIR (total 29)</u>						
A		2	2		2	
A to CT			3			2
CT		2				5
CT to Q				8		
Q				3		
<u>Interpreted (total 30)</u>						
A	3	7	1 [†]		11	
A to CT			2			
CT		5				
CT to Q						1
Q						
* A – opal-A, A to CT – opal-A to opal-CT transition, CT – opal-CT, CT to Q – opal-CT to quartz transition, and Q – diagenetic quartz						
[†] Heated to 156 °C by field-based steam operations						

Samples interpreted as opal-A to opal-CT transition group members, B 1432.7 and B 1432.9, are from a different well than the other Field B samples (Tables 4–5 in Ross and Kovscek, 2022). All of the Field B samples from a depth of about 1400 to 1440 feet exhibit an opal-A SEM texture, which could represent either opal-A or opal-A to opal-CT transition groups (Table 2 in Ross and Kovscek, 2022). Samples from this depth range with quantitative XRD contain 1 to 11 wt% opal-CT (Table 3 in Ross and Kovscek, 2022). Based on our experience with Field B samples, B 1432.7 and B 1432.9 were assigned to the opal-A to opal-CT transition group. This is supported by the similarity between the MIP and sorption results of all Field B samples (with known and interpreted silica group status) from this depth range as shown in Figures 1 and A1 in Ross and Kovscek (2022). If this had not been the case, XRD spectra would have been generated.

All of the interpreted opal-CT group members are from the same Field A well (Table 5 in Ross and Kovscek, 2022). Samples A 992.0, A 1011.0, A 1013.8, A 1017.0, and A 1019.0 exhibit an opal-CT SEM texture, which is indicative of both opal-CT and opal-CT to quartz transition groups (Table 2 in Ross and Kovscek, 2022; Fig. S7). The opal-CT classification is supported by XRD spectra as well as quantitative XRD results of adjacent samples, A 1009.7 and A 1015.0 (Table 3 in Ross and Kovscek, 2022). This is substantiated via similarities in their nanometer-scale pore structures for all Field A samples classified in the opal-CT silica group. The interpreted opal-CT to quartz transition sample, E 823.9, was classified via imaging of SEM

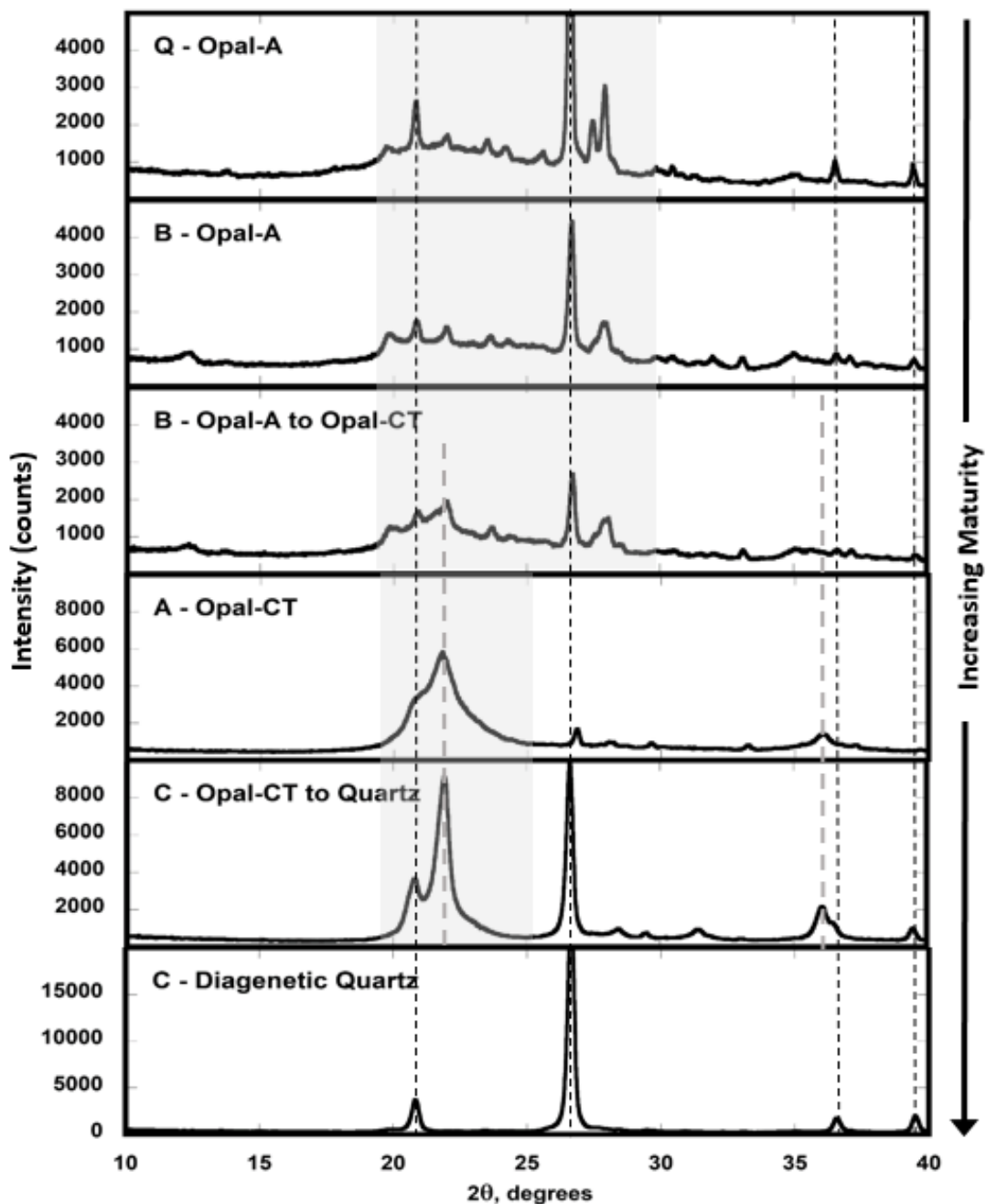


Figure S8. Representative powder X-ray diffraction (XRD) spectra excerpts for each silica group listed by increasing silica maturity (arrow). Letters indicate sample source (either quarry or field). Amorphous phase regions for opal-A and opal-CT are shaded. Gray dashed lines indicate opal-CT peaks. Black dashed lines denote quartz peak locations. Peak locations are from Smith (1998) and Rice et al. (1995). Unlabeled notable peaks in these examples are contributed by feldspars in the three uppermost samples; these samples contain detrital grains.

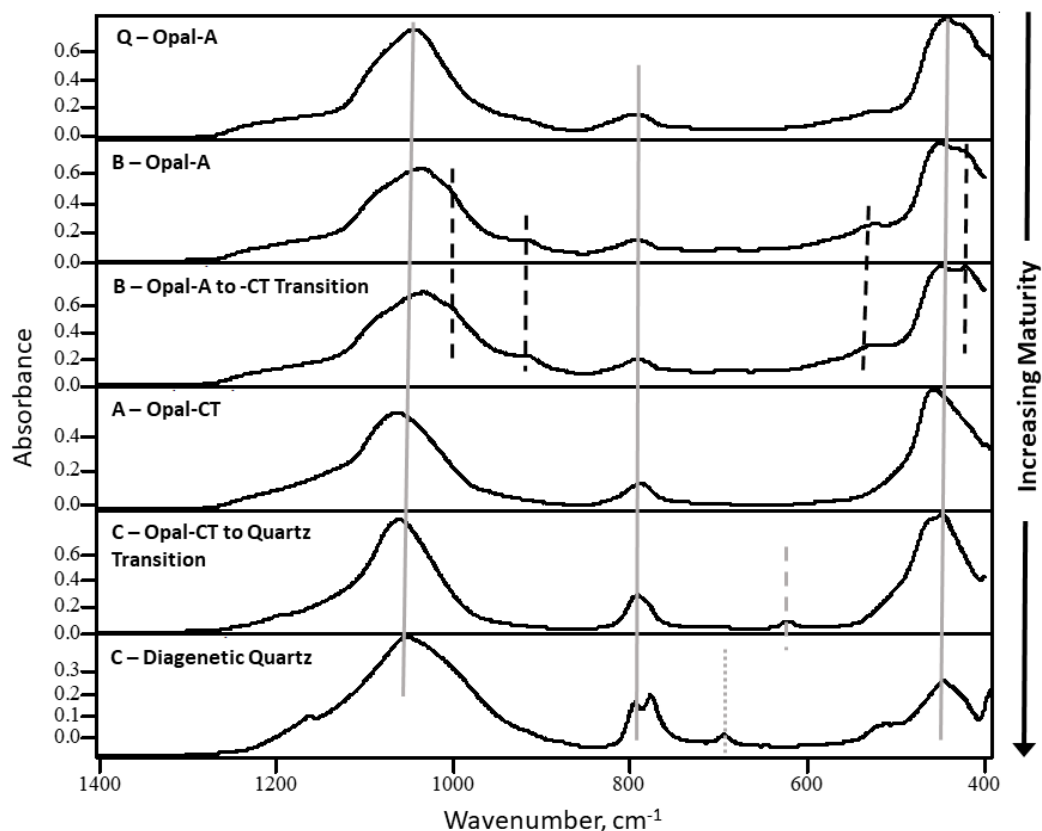


Figure S9. Example Fourier transform infrared (FTIR) absorbance spectra excerpts for each silica group in order of increasing silica maturity (arrow). Peaks associated with silica (gray lines) and clays (black dashed lines) are labeled. Letters indicate the sample source of either quarry (Q) or field. Field B examples are clay-rich. The silica peak at 623 cm^{-1} is associated with opal-C (disordered cristobalite; dashed gray line) whereas the silica peak at 693 cm^{-1} occurs only in the fully converted diagenetic quartz (dotted gray line). Peak locations are from Gadsden (1975) and Rice et al. (1995).

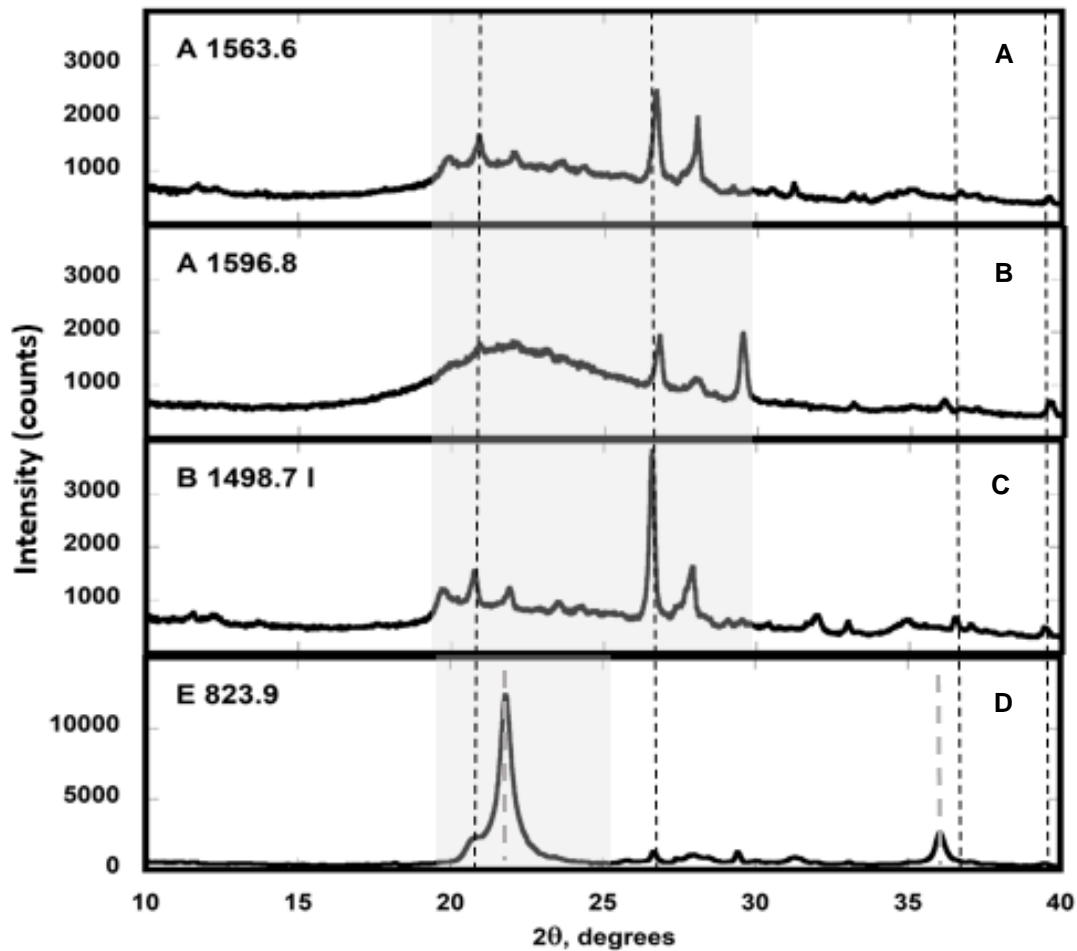


Figure S10. Powder XRD spectra excerpts for select samples. Labels are sample names indicating source (field) and burial depth. Amorphous phase regions for opal-A and opal-CT are shaded. Gray dashed lines indicate opal-CT peaks. Black dashed lines denote quartz peak locations except when associated with opal-CT at $\sim 21^\circ 2\theta$ and lacking a substantial peak between 26 and $27^\circ 2\theta$ (E 823.9). Unlabeled notable peaks are contributed by feldspars except for the calcite peak between 29 and $30^\circ 2\theta$ for A 1596.8.

mounts, spectral XRD, and FTIR (Fig. S10D; Table 5 in Ross and Kavscek, 2022). This is particularly true for FTIR in that opal-CT to quartz group members are uniquely identified by an opal-C FTIR peak at 623 cm^{-1} . Additional sorption data and SEM images in the format as Fig. 4 in Ross and Kavscek (2022) are presented in Figure S11. Figure S12 contains supplemental SEM images. These figures occur in later sections.

COMPARISON WITH OTHER WORK

Sorption measurements of Monterey Formation samples are rare in the literature. Most of the papers are tied to measurements conducted at Colorado School of Mines. Godinez (2014) conducted nitrogen sorption measurements on a quartz porcelanite and two opal-CT porcelanite

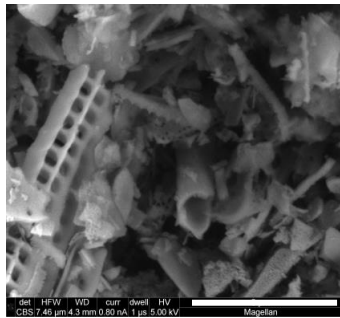
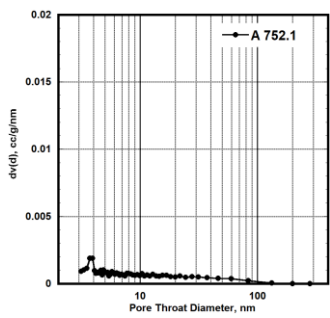
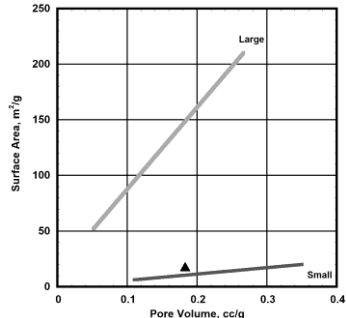
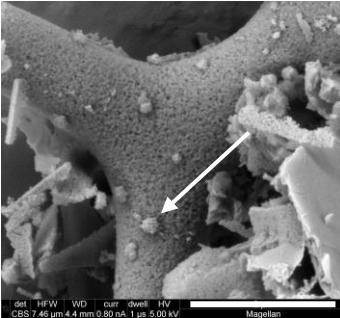
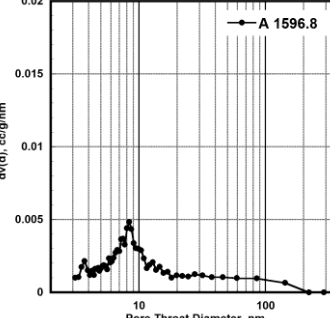
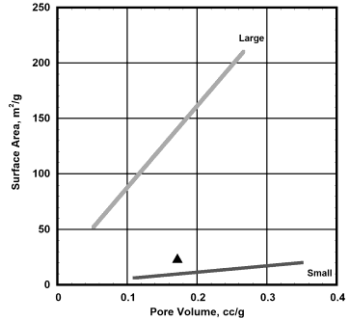
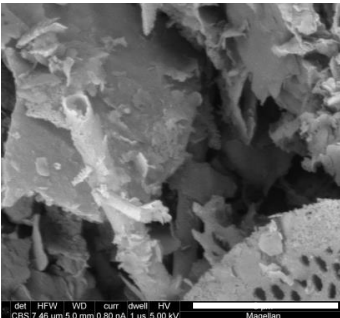
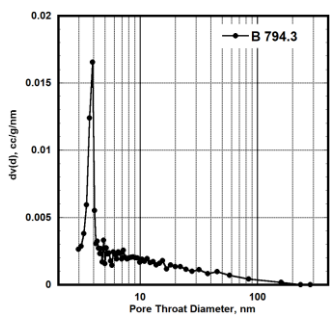
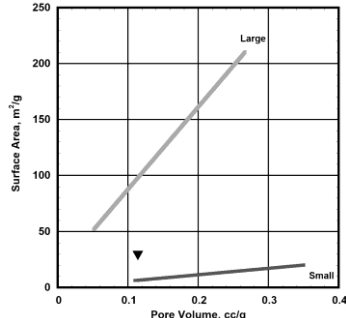
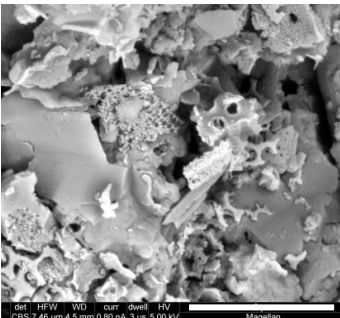
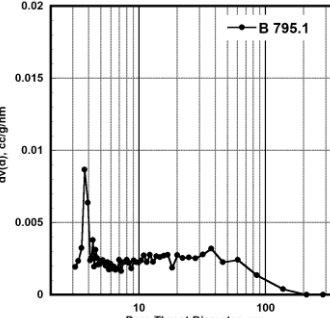
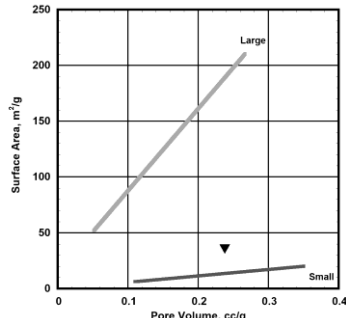
samples. In the detailed methodology of Godinez (2014), the samples were crushed and sieved to 420 μm and smaller. Prior to nitrogen sorption, these samples were outgassed at 110 $^{\circ}\text{C}$. The samples were not cleaned to remove soluble hydrocarbons. Subsequent papers from this group were published on quartz porcelanite samples (e.g., Saidian et al., 2014, 2016). Yuan and Rezaee (2019) incorporate the nitrogen sorption plot from Saidian et al. (2016). These later papers used an outgassing temperature of 200 $^{\circ}\text{C}$ on crushed samples ($\leq 420 \mu\text{m}$). Based on the isotherm data provided in Godinez (2014), 50 points were collected on adsorptive branch and 40 points were collected on the desorptive branch. These papers used the BJH method (Barrett et al., 1951) with thickness determined using the Harkins and Jura (1944) method. The thickness method was not specified in Godinez (2014). The results were plotted as $dv/d\log(d)$. Surface area is provided in plots and sometimes in tables. Sorption-based pore volumes were not provided.

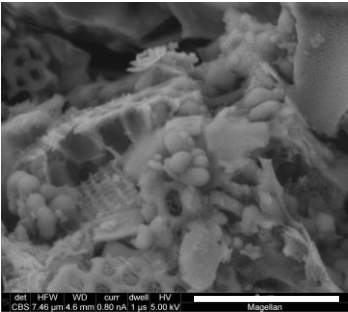
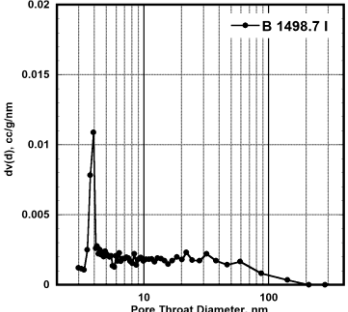
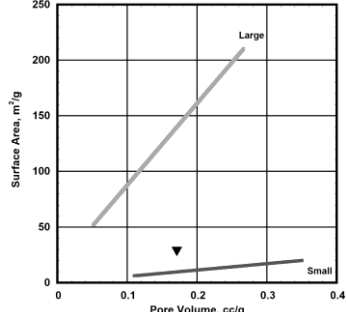
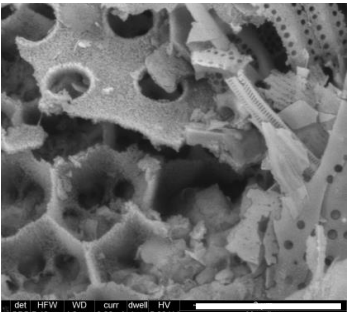
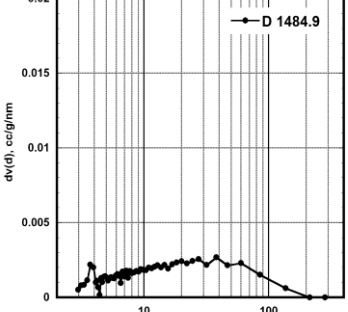
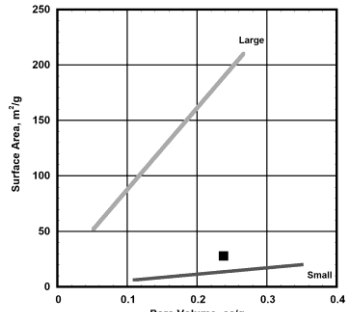
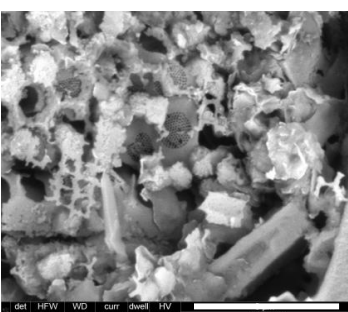
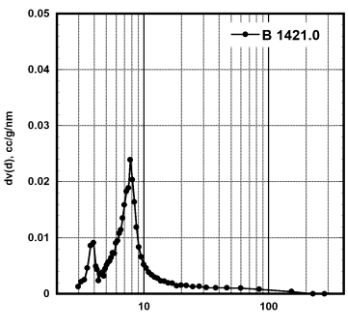
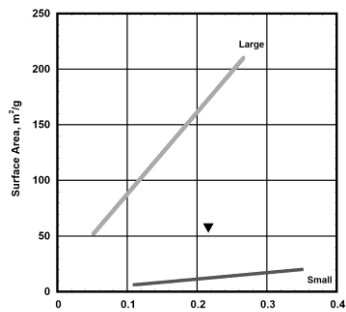
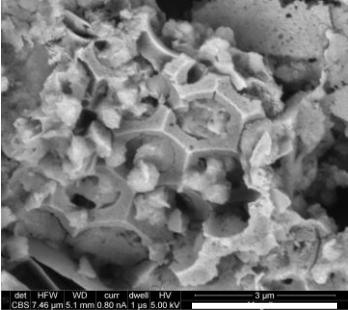
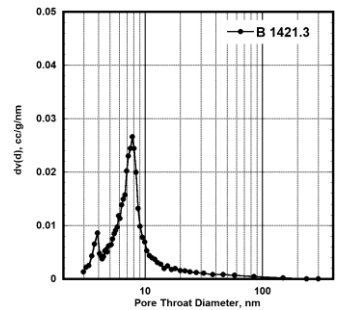
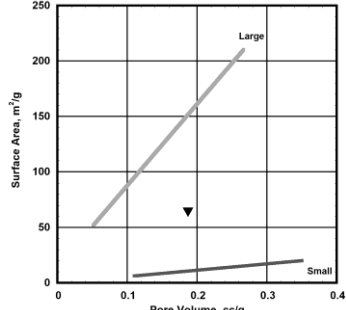
For comparison, select opal-CT and quartz porcelanites from this study were plotted as $dv/d\log(d)$ (not shown). The nitrogen sorption measurements of opal-CT porcelanites using their methodology have peaks in the 10–100 nm diameter range (Figs. 5–12 in Godinez, 2014). The peak magnitudes are similar to those encountered in this study (e.g., 0.6 cm^3/g). For quartz porcelanites, the peak heights are much less (e.g., 0.002–0.02 cm^3/g) in Godinez (2014) than in this study (e.g., 0.03–0.05 cm^3/g). All of the distributions in Godinez (2014) are missing the first peak reported in this study. One sample reported in Saidian et al. (2016) exhibits this peak. Surface areas for the opal-CT porcelanites of Godinez (2014) fall with the range reported for the opal-CT to quartz group members of this study whereas the quartz porcelanites have nSA values equivalent to diagenetic quartz group members (Fig. 5 in Ross and Kavscek, 2022).

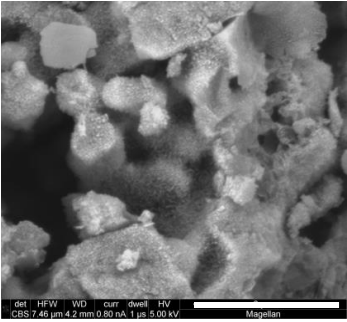
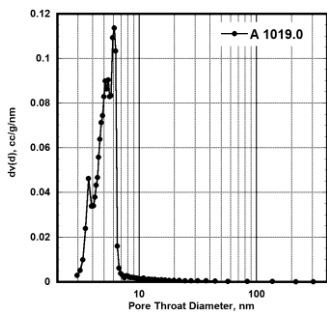
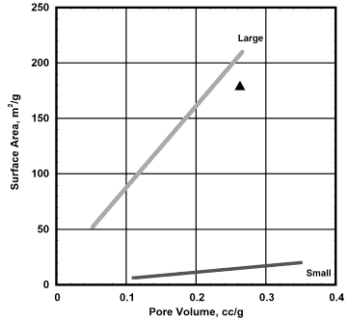
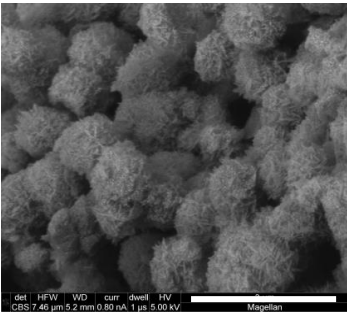
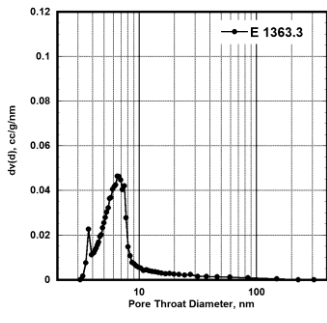
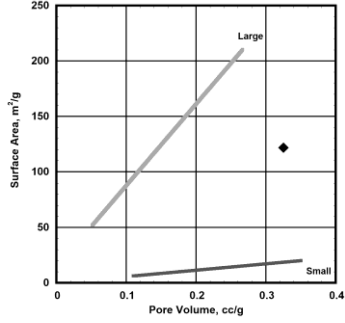
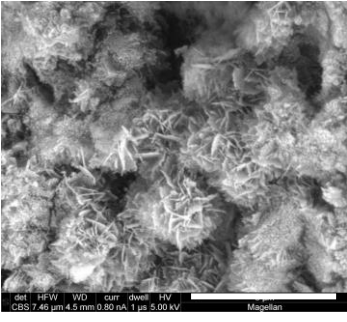
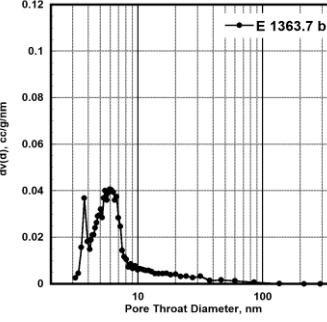
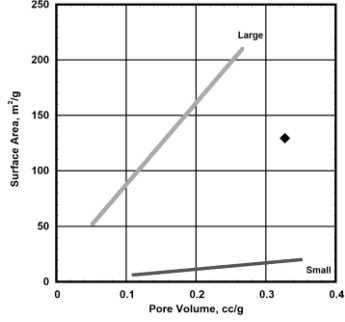
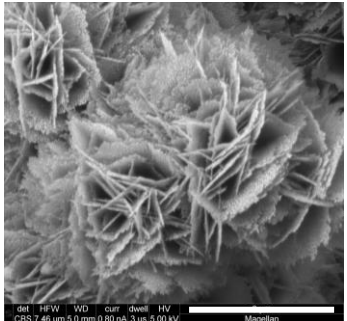
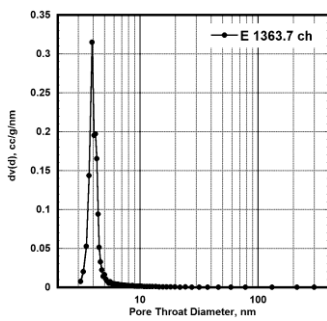
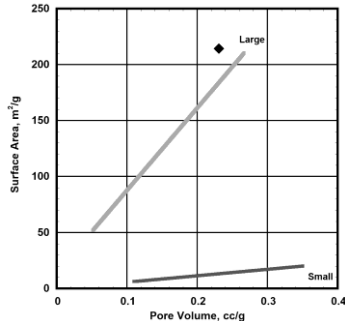
Discrepancies between this work and these previously published sorption work on Monterey Formation samples are attributed to differences between the study samples as well as sample preparation and analysis methods (e.g., cleaning, sample size, outgassing temperature, and number of data points). For example, the opal-CT and quartz porcelanite samples of this study have much lower carbonate and clay compositions compared to Godinez's (2014) samples. This explains the lower pore volumes in the nPSD in that the nanoporosity of opal-CT is expressed per gram of sample material. In addition, missing first peaks are attributed to extreme dissolution as explained previously, but this can result from an insufficient number of measured sample points for the sorption isotherms. The additional steps allow more time for the pores to fill and drain during the sorption measurements. Lack of cleaning, outgassing temperature, and reservoir conditions (if applicable) could also play a role.

Dasani (2017) also performed nitrogen sorption on a quartz porcelanite with a reported nSA of 6.62 m^2/g and nPV of 0.027 cm^3/g . These values are about half that reported in this study (Table 4 in Ross and Kavscek, 2022). Details on cleaning, sample size, outgassing, and data collection settings were not provided. As in the other studies, this quartz porcelanite contains more clay (18 wt%) than our study samples (3 wt%; Table 3 in Ross and Kavscek, 2022).

ADDITIONAL SEM IMAGE AND PORE STRUCTURE EXAMPLES

Silica Group	Morphology	nPSD (+ sample name)	nPV vs nSA (+ trend locations)
Opal-A			
Opal-A			
Opal-A			
Opal-A			

Silica Group	Morphology	nPSD (+ sample name)	nPV vs nSA (+ trend locations)
Opal-A*			
Opal-A			
Opal-A to Opal-CT			
Opal-A to Opal-CT			

Silica Group	Morphology	nPSD (+ sample name)	nPV vs nSA (+ trend locations)
Opal-CT			
Opal-CT			
Opal-CT			
Opal-CT			

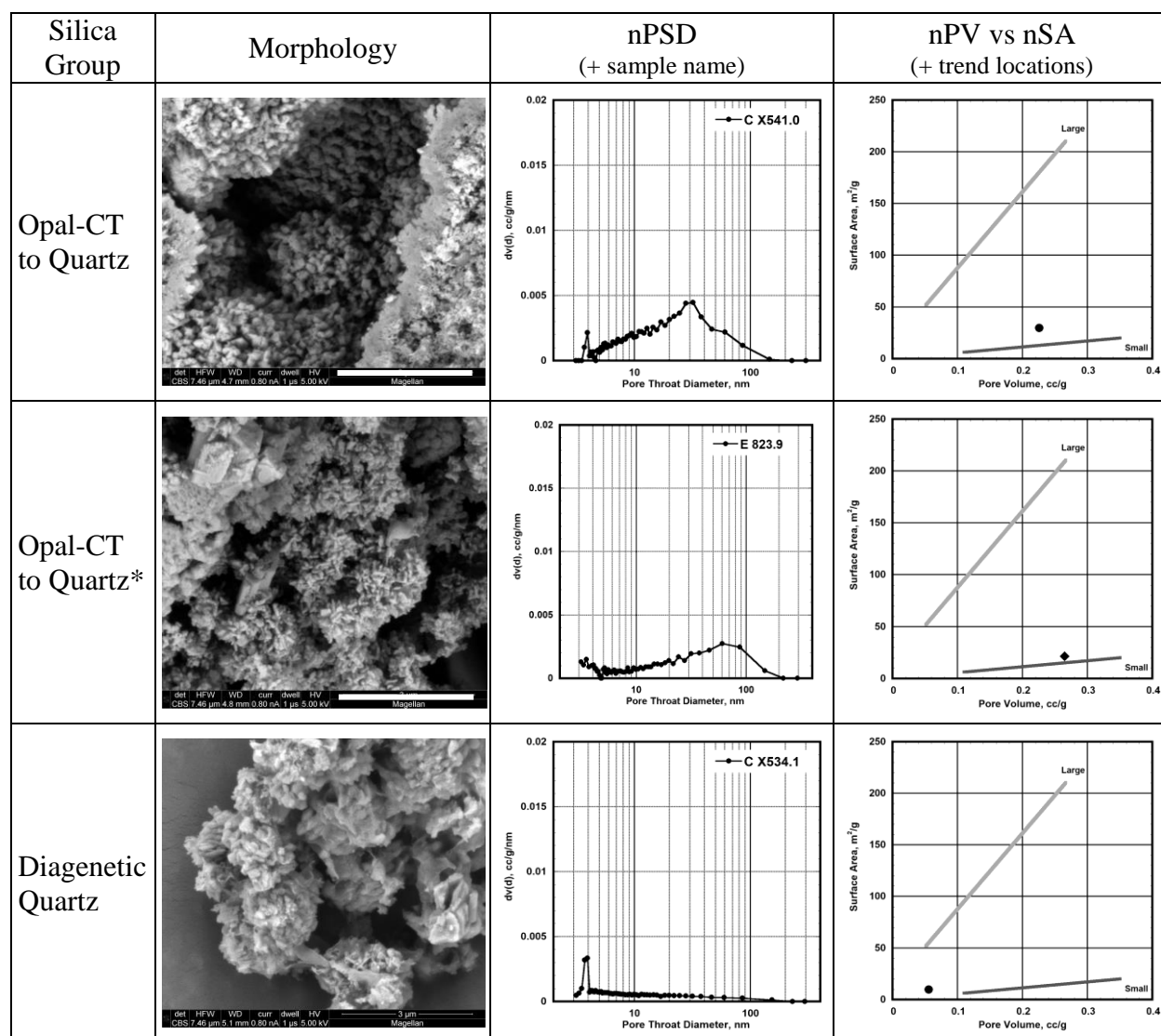
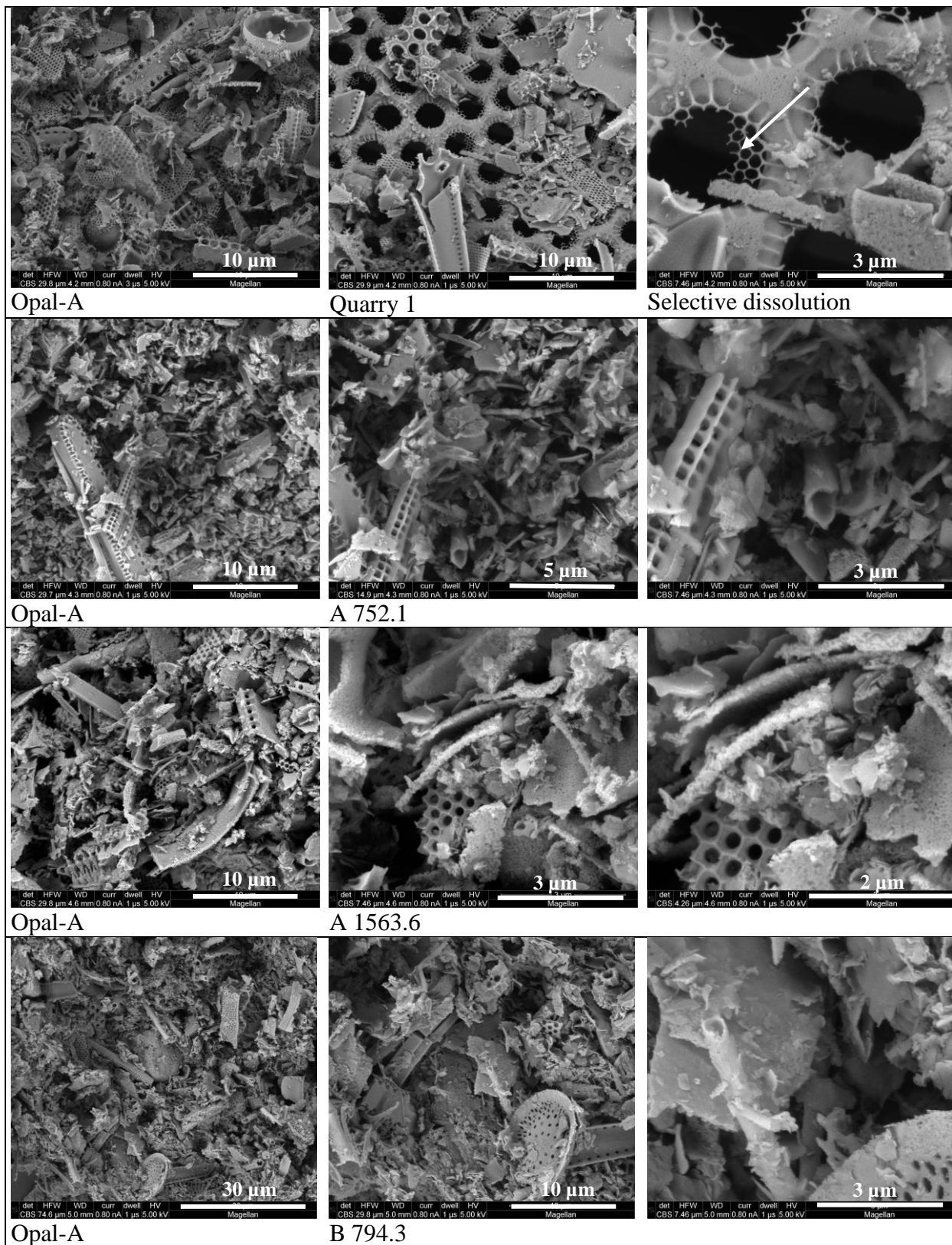
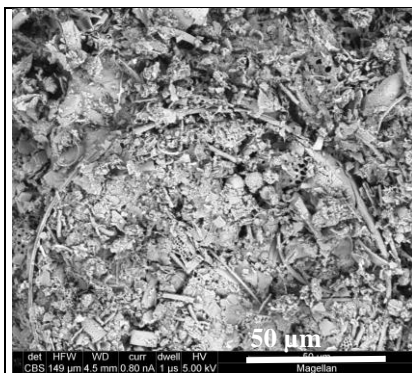


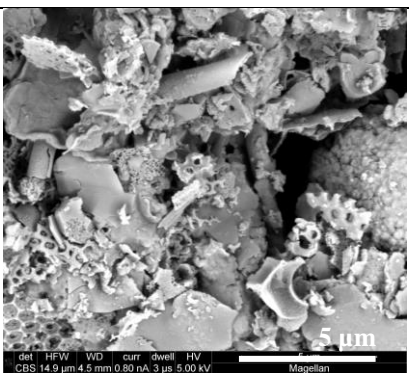
Figure S11. Additional representative samples per silica group (left column), scanning electron microscopy (SEM) photomicrographs (Morphology column), nPSD, and nPV-nSA crossplots, respectively. Samples are ordered by silica group in order of increasing maturity from opal-A to diagenetic quartz silica groups. Within each silica group, samples are ordered alphabetically by sample name. Each row represents the sample named in the nPSD legend. The vertical scale is variable for nPSD plots. The reference lines in the nPV-nSA scatterplots are in the same locations as in Figures 3 and 4 in Ross and Kavscek (2022). All SEM images were collected at the same magnification. Scale bars are 3 μm . Additional examples are in Figure 4 in Ross and Kavscek (2022). (* In-situ alteration due to field operations. Further details for these samples are provided in Ross and Kavscek, 2022.)

ADDITIONAL SEM IMAGES

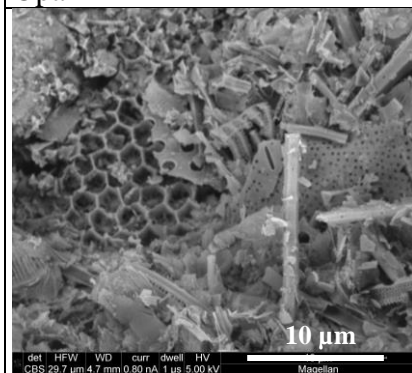
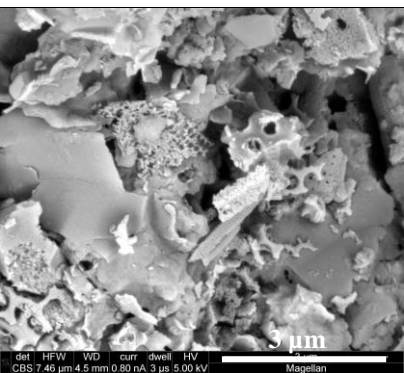




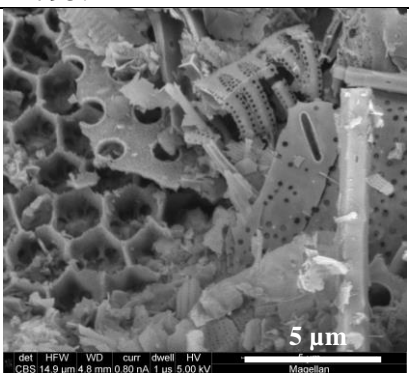
Opal-A



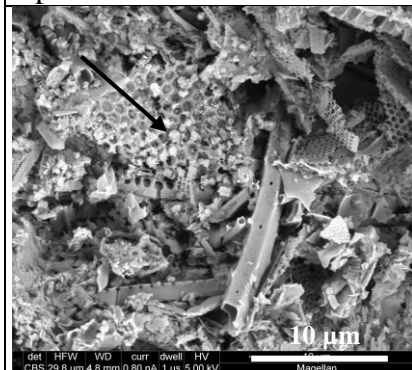
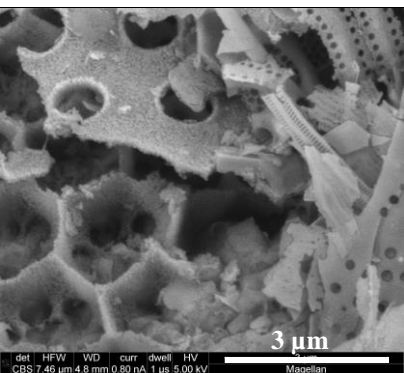
B 795.1



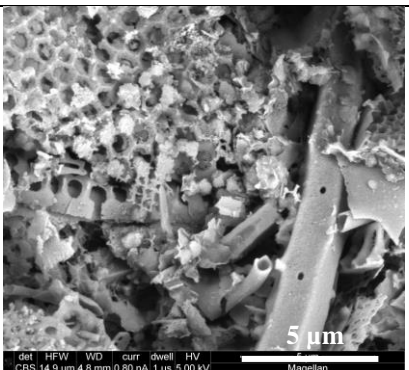
Opal-A



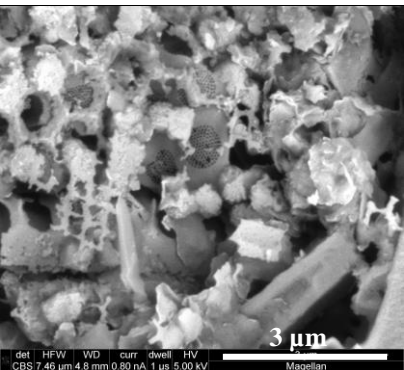
D 1484.9



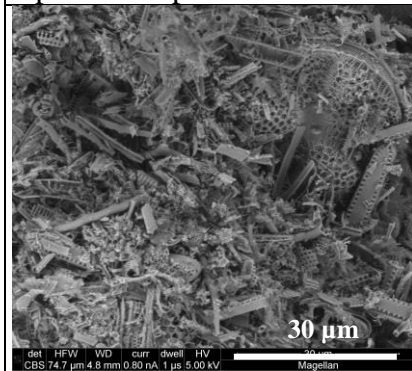
Opal-A to Opal-CT Transition



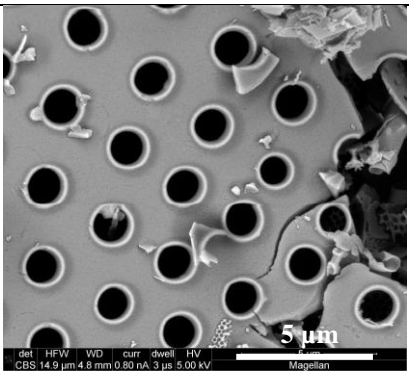
B 1421.0



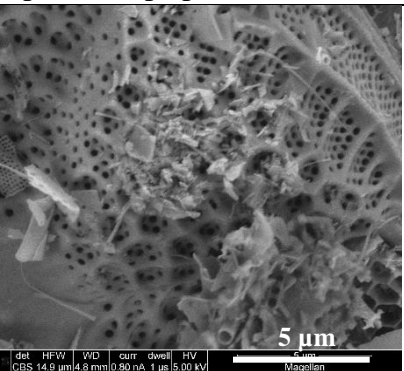
Opal-CT lepispheres



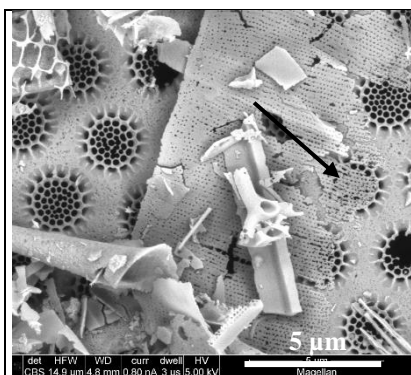
Opal-A to Opal-CT Transition



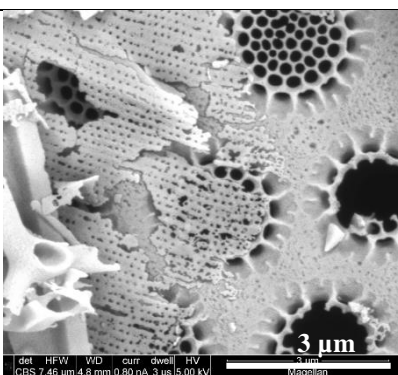
E 1224.6



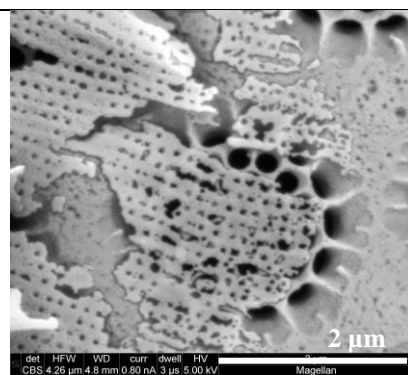
No apparent dissolution



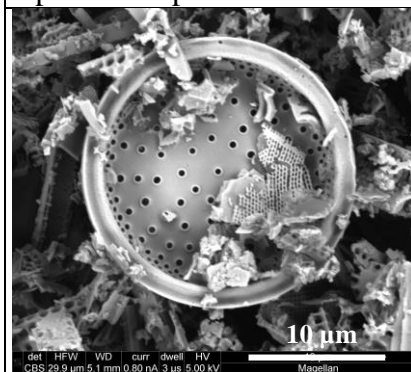
Opal-A to Opal-CT Transition



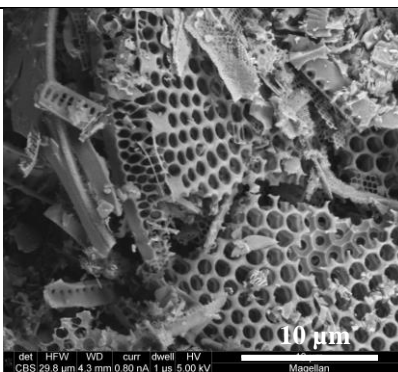
E 1224.6



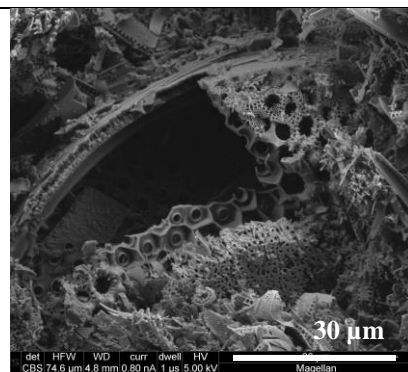
Selective dissolution



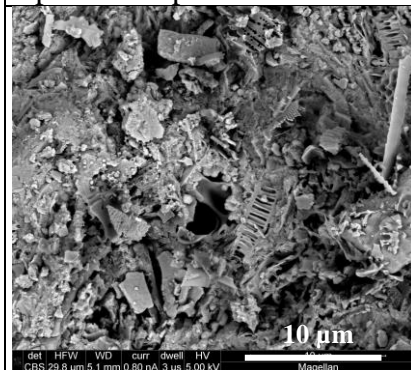
Opal-A to Opal-CT Transition



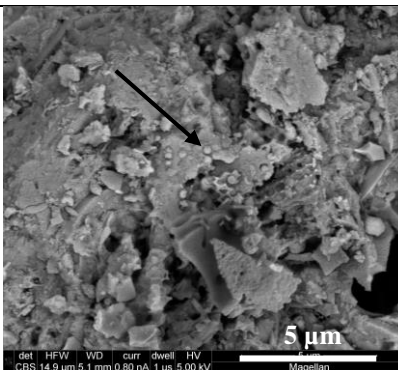
E 1225.3



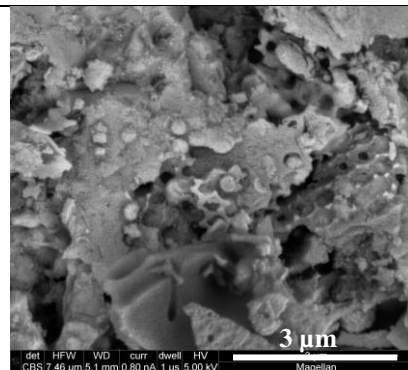
Selective dissolution



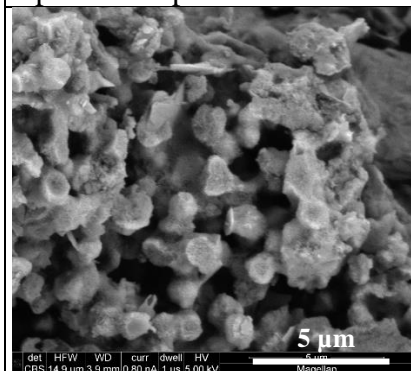
Opal-A to Opal-CT Transition



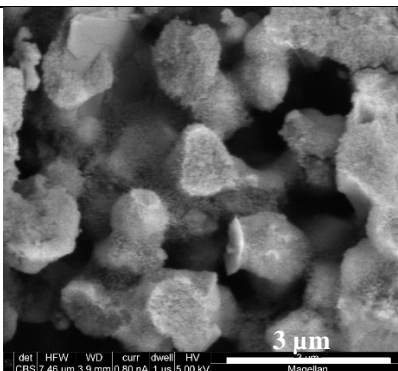
E 1225.3



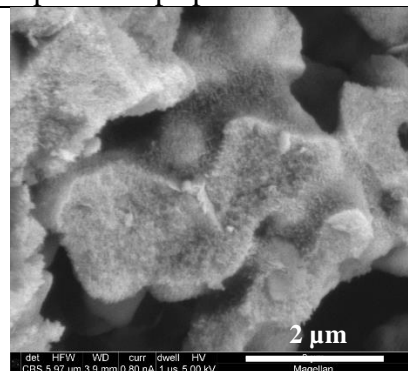
Opal-CT lepispheres



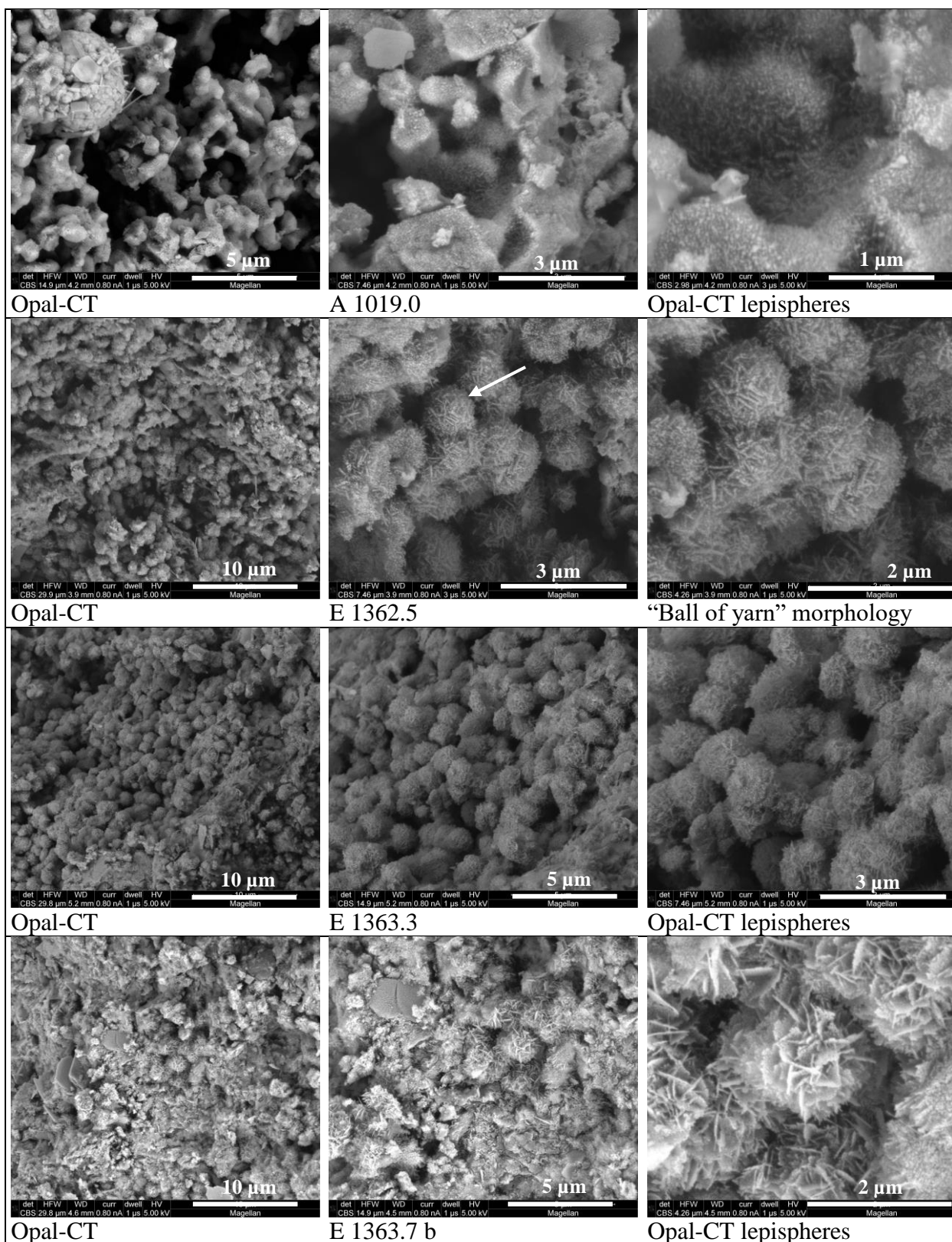
Opal-CT



A 1009.7



Opal-CT lepispheres



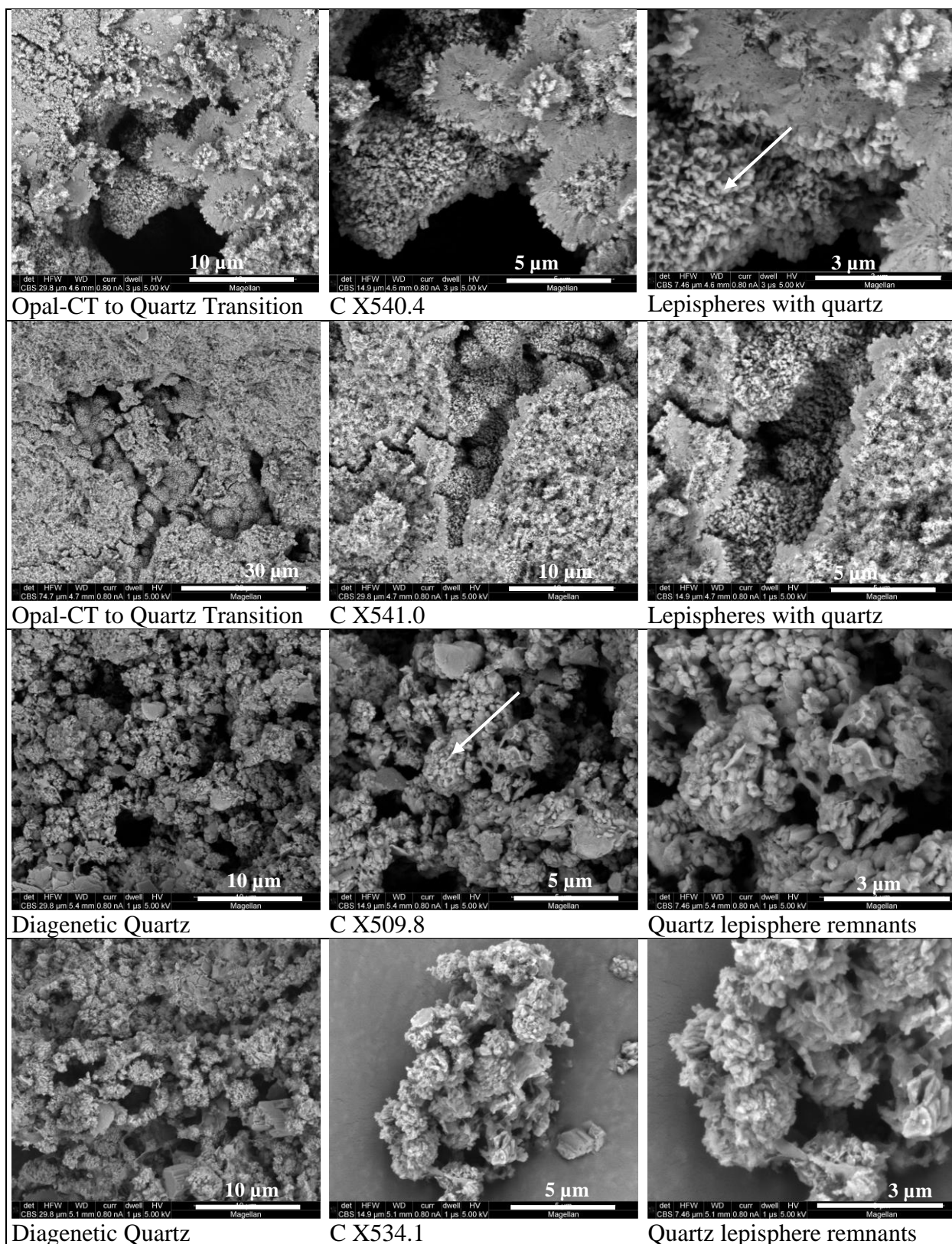


Figure S12. Scanning electron microscopy (SEM) photomicrographs for select samples. Samples are arranged by silica group by increasing silica maturity followed by sample name in

alphabetical order. Images within a row are from the same sample. A few samples have multiple rows. Listed beneath the SEM images, the silica group is in first column, sample name is in the middle column, and comments are in the last column. Magnification and the size of the scale bars vary. For the most part, lowest magnification images are in the first column, highest magnification images are in the third column, and intermediate magnifications are in the center column. Arrows and circles, in most cases, designate the first occurrence of features named in the last column of the row. Additional images are in Figure A2 in Ross and Kovsky (2022).

ACKNOWLEDGMENTS

This work was undertaken with the support of Stanford University Petroleum Research Institute (SUPRI-A) Industrial Affiliates. Part of this work was conducted in the Stanford Nano Shared Facilities (SNSF), which is supported by the NSF as part of the National Nanotechnology Coordinated Infrastructure under award ECCS-2026822. Additional work was performed in the SUPRI-A, Benson, SUMAC, and MAF laboratories of the School of Earth, Energy, and Environmental Sciences, Stanford University. Matt Tilghman, formerly part of the Thermosciences Group at Stanford University, performed the TGA measurements. Portions of this Supplemental Material were presented at the Society of Petroleum Engineers Western Regional Meeting held in Anchorage, Alaska, 23 to 26 May 2016 and are used with permission of the Society of Petroleum Engineers to republish via the Copyright Clearance Center.

REFERENCES

- Barrett, E.P., Joyner, L.G., and Halenda, P.P., 1951, The determination of pore volume and area distributions in porous substances. I. Computations from nitrogen isotherms: *Journal of the American Chemical Society*, v. 73, p. 373–380, <https://doi.org/10.1021/ja01145a126>.
- Dasani, D., 2017, Investigation of mass transfer in fractured shales [Ph.D. thesis]: University of Southern California, 183 p.
- de Boer, J.H., Lippens, B.C., Linsen, B.G., Broekhoff, J.C.P., van den Heuvel, A., and Osinga, T.J., 1966, The *t*-curve of multimolecular N₂ adsorption: *Journal of Colloid and Interface Science*, v. 21, no. 4, p. 405–414, [https://doi.org/10.1016/0095-8522\(66\)90006-7](https://doi.org/10.1016/0095-8522(66)90006-7).
- Gadsden, J.A., 1975, *Infrared Spectra of Minerals and Related Inorganic Compounds*: London, Butterworths, 277 p.
- Godinez, L.J., 2014, Important mineralogical factors for fluid saturation, specific surface area and pore size distributions based on gas adsorption, cation exchange capacity and 2D dielectric microscopy: A case study of quartz phase porcelanites in the Miocene Monterey Formation [M.S. thesis]: Colorado School of Mines, 133 p.

- Harkins, W.D., and Jura, G., 1944, Surfaces of solids. XIII. A vapor adsorption method for the determination of the area of a solid without the assumption of a molecular area, and the areas occupied by nitrogen and other molecules on the surface of a solid: *Journal of the American Chemical Society*, <https://doi.org/10.1021/ja01236a048>.
- Ikeda, M., Tang, G.-Q., Ross, C.M., and Kovsky, A.R., 2007, Oil recovery and fracture reconsolidation of diatomaceous reservoir rock by water imbibition at elevated temperature: Paper presented at the Society of Petroleum Engineers Annual Technical Conference and Exhibition, Anaheim, CA, 11–14 November, 21 p., <https://doi.org/10.2118/110515-MS>.
- Joyner, L.G., Barrett, E.P., and Skold, R., 1951, The determination of pore volume and area distributions in porous substances. II. Comparison between nitrogen isotherm and mercury porosimeter methods: *Journal of the American Chemical Society*, v. 73, p. 3155–3158, <https://doi.org/10.1021/ja01151a046>.
- Klobes, P., Meyer, K., and Minro, R.G., 2006, Porosity and specific surface area measurements for solid materials: NIST - National Institute of Standards and Technology, v. 50, p. 1175–93, <http://doi.org/682901795>.
- Kuila, U., and Prasad, M., 2013, Specific surface area and pore-size distribution in clays and shales: *Geophysical Prospecting*, v. 61, p. 341–362, <https://doi.org/10.1111/1365-2478.12028>.
- Lowell, S., Shields, J.E., Thomas, M.A., and Thommes, M., 2004, Characterization of porous solids and powders: Surface area, pore size and density: Particle Technology Series, Kluwer Academic Publishers, Norwell, Massachusetts, 349 p., <https://doi.org/10.1007/978-1-4020-2303-3>.
- Mielenz, R.C., Schieltz, N.C., and King, M.E., 1953, Thermogravimetric analysis of clay and clay-like minerals: *Clays and Clay Minerals*, v. 2, no. 1, p. 285–314, <https://doi.org/10.1346/CCMN.1953.0020124>.
- Peng, J., and Kovsky, A.R., 2011, Temperature-induced fracture reconsolidation of diatomaceous rock during forced water imbibition: *Society of Petroleum Engineers Reservoir Evaluation and Engineering*, v. 14, no. 01, p. 45–59, <https://doi.org/10.2118/132411-PA>.
- Rice, S.B., Freund, H., Huang, W.-L., Clouse, J.A., and Isaacs, C.M., 1995, Application of Fourier transform infrared spectroscopy to silica diagenesis: the opal-A to opal-CT transformation: *Journal of Sedimentary Research*, v. A65, no. 4, p. 639–647, [10.1306/D4268185-2B26-11D7-8648000102C1865D](https://doi.org/10.1306/D4268185-2B26-11D7-8648000102C1865D).
- Ross, C.M., Ikeda, M., Tang, G.-Q., and Kovsky, A.R., 2008, Alteration of reservoir diatomites by hot water injection: Paper presented at the SPE Western Regional Meeting and Pacific Section AAPG Joint Meeting, Bakersfield, California, 29 March–4 April, 13 p., <https://doi.org/10.2118/114183-MS>.

- Ross, C.M., and Kovscek, A.R., 2022, this volume, Nanometer-scale pore structure and the Monterey Formation: A new tool to investigate silica diagenesis, *in* Aiello, I., Barron, J., and Ravelo, C., eds., *Understanding the Monterey Formation and Similar Biosiliceous Units across Space and Time: Geological Society of America Special Paper 556*, [https://doi.org/10.1130/2022.2556\(04\)](https://doi.org/10.1130/2022.2556(04)).
- Ross, C.M., Vega, B., Peng, J., Ikeda, M., Lagasca, J.R.P., Tang, G.-Q., and Kovscek, A.R., 2016, Detecting opal-CT formation resulting from thermal recovery methods in diatomites: Paper presented at the Society of Petroleum Engineers Western Regional Meeting held in Anchorage, Alaska, 23–26 May, p. 1–32, <https://doi.org/10.2118/180369-MS>.
- Saidian, M., Kuila, U., Rivera, S., Godinez, L.J., and Prasad, M., 2014, Porosity and pore size distribution in mudrocks: A comparative study for Haynesville, Niobrara, Monterey and Eastern European Silurian formations: Paper presented at the Society of Petroleum Engineers - SPE/AAPG/SEG Unconventional Resources Technology Conference, p. 1226–1243, <http://doi.org/10.15530/urtec-2014-1922745>.
- Saidian, M., Kuila, U., Prasad, M., Barraza, S.R., Godinez, L.J., and Alcantar-Lopez, L., 2016, A comparison of measurement techniques for porosity and pore size distribution in shales (mudrocks): A case study of Haynesville, Eastern European Silurian, Niobrara, and Monterey formations: AAPG Memoir, v. 112, p. 89–144, <https://doi.org/10.1306/13592019M1123695>.
- Sing, K.S.W., Everett, D.H., Haul, R.A.W., Moscou, L., Pierotti, R.A., Rouquerol, J., and Siemienwska, T., 1985, Reporting physisorption data for gas/solid systems with special reference to the determination of surface area and porosity: *Pure and Applied Chemistry*, v. 57, no. 4, p. 603–619, <https://doi.org/10.1351/pac198557040603>.
- Smallwood, A.G., Thomas, P.S., and Ray, A.S., 2008, The thermophysical properties of Australian opal: *Proceedings of the 9th International Congress for Applied Mineralogy*, Brisbane, Queensland, 8–10 September: Australasian Institute of Mining & Metallurgy, p. 557–560.
- Smith, D.K., 1998, Opal, cristobalite, and tridymite: Noncrystallinity versus crystallinity, nomenclature of the silica minerals and bibliography: *Powder Diffraction*, v. 13, p. 2–19, <https://doi.org/10.1017/S0885715600009696>.
- Tourtelot, H.A., 1979, Black shale – Its deposition and diagenesis: *Clays and Clay Minerals*, v. 27, no. 5, p. 313–321, <https://doi.org/10.1346/CCMN.1979.0270501>.
- Vega, B., and Kovscek, A.R., 2010, The effect of temperature and oil viscosity reduction on water imbibition of diatomite: Paper presented at the Society of Petroleum Engineers Western North American Regional Meeting held in Anaheim, California, 27–29 May, p. 669–682, <http://dx.doi.org/10.2118/133132-MS>.
- Vega, B., and Kovscek, A.R., 2014, Steady-state relative permeability measurements, temperature dependency and a reservoir diatomite core sample evolution: Paper presented at the Society of Petroleum Engineers Annual Technical Conference and Exhibition held in

Amsterdam, The Netherlands, 27–29 October, 14 p., p. 4471–4484,
<http://dx.doi.org/10.2118/170918-MS>.

Vega, B., Tang, G.Q., and Kovscek, A.R., 2011, Thermally induced fracture reconsolidation of diatomite under no flow conditions: Paper presented at the Society of Petroleum Engineers Western North American Regional Meeting held in Anchorage, Alaska, 7–11 May, p. 239–248, <https://doi.org/10.2118/144525-MS>.

Yuan, Y., and Rezaee, R., 2019, Comparative porosity and pore structure assessment in shales: Measurement techniques, influencing factors and implications for reservoir characterization: *Energies*, v. 12, n. 11, 2094, 14 p., <https://doi.org/10.3390/en12112094>.

Zhuravlev, L.T., 2000, The surface chemistry of amorphous silica. Zhuravlev Model: Colloids and Surfaces. A, Physicochemical and Engineering Aspects, v. 173, p. 1–38,
[https://doi.org/10.1016/S0927-7757\(00\)00556-2](https://doi.org/10.1016/S0927-7757(00)00556-2).